JOURNAL OF PETROLOGY | VOLUME 36 | NUMBER 5 | PAGES 1137–1170 | 1995

M. J. TOPLIS* AND M. R. CARROLL
DEPARTMENT OF GEOLOGY, UNIVERSITY OF BRISTOL, BRISTOL BS8 1RJ, UK

An Experimental Study of the Influence of Oxygen Fugacity on Fe–Ti Oxide Stability, Phase Relations, and Mineral–Melt Equilibria in Ferro-Basaltic Systems

Equilibrium crystallization experiments at atmospheric pressure and over a range of oxygen fugacity (f_{O_2}) have been carried out on a ferro-basaltic composition similar to liquids proposed to have been parental to much of the exposed portion of the Skaergaard intrusion. Before Fe–Ti oxide saturation the liquid line of descent is little affected by f_{O_2}. However, the appearance temperatures of the magnetite–ulvöspinel solid solution (Mt) and the ilmenite–haematite solid solution (Ilm) depend strongly on f_{O_2}. Above the fayalite–magnetite–quartz (FMQ) buffer Mt is the first oxide phase to appear on the liquidus, but below the FMQ buffer Ilm is the first oxide to crystallize. The appearance temperature of Mt is ~1100°C at FMQ, and the Mt liquidus slope is ~30°C/log f_{O_2} unit between FMQ − 2 and FMQ + 1. The Ilm liquidus is at ~1100°C between FMQ and FMQ − 2, but moves to lower temperature at higher f_{O_2} where Mt is the first oxide phase. The results indicate that the ferric iron content of Mt-saturated melts varies linearly with inverse temperature, and that Ilm saturation is closely related to melt TiO_2 content. Mt saturation produces an immediate enrichment of SiO_2 and depletion in FeO in the melt phase, whereas Ilm saturation produces similar enrichment in SiO_2, but iron enrichment may continue for ~10°C below the ilmenite liquidus. The experimental liquids reach a maximum of ~18 wt % FeO*, at ~48 wt % SiO_2 for ilmenite-saturated melts at low f_{O_2}, more differentiated melts having lower iron and higher silica. Cotectic proportions, derived from mass balance calculations, are in good agreement with data from natural samples and other experimental studies. Olivine resorption is inferred at all f_{O_2} with the onset of resorption occurring ~10°C higher than the appearance of magnetite. The effect of f_{O_2} on silicate mineral compositions, and partitioning of elements between coexisting mineral–melt pairs, is small. Thermodynamic considerations suggest that variations of Fe–Mg partitioning between the iron-rich olivines, pyroxenes and melts produced in this study may be explained by known non-idealities of Fe–Mg mixing in the crystalline phases, rather than non-idealities in the coexisting melts. These experiments also provide insights into many features common to natural tholeiitic series of volcanic and plutonic rocks, and provide experimental data required for modelling of fractional crystallization and crystallization closed to oxygen, processes which are not easily investigated experimentally.*

KEY WORDS: *ferro-basalt; Fe–Ti oxides; oxygen fugacity; Skaergaard intrusion; iron enrichment*

INTRODUCTION

It is generally accepted that low-pressure crystallization of sub-alkaline basalts yields a tholeiitic differentiation trend characterized by iron enrichment in the melt phase during the early stages of crystallization, followed by enrichment in silica and depletion in iron at higher degrees of differentiation. Natural systems show a continuum of differentiation trends from calk-alkaline to tholeiitic, but the maximum extent of iron enrichment possible, and the factors which control it, are not well understood. Volcanic tholeiitic suites typically show iron enrichment in the melt phase to ~15 wt % FeO* before the formation of more silica-rich products (e.g. Thingmuli, Iceland; Carmichael, 1964). More

*Corresponding author. Present address: Bayerisches Geoinstitut, Universität Bayreuth, D-95440 Bayreuth, Germany

recently, melt FeO* contents of up to ~19 wt% have been found in evolved, but still broadly basaltic, submarine glasses from divergent plate margins such as the Galapagos spreading centre (e.g. Byerly, 1980; Le Roex *et al.*, 1982; Fornari *et al.*, 1983; Brooks *et al.*, 1991). Even greater iron enrichments have been proposed to have occurred during the formation of the Skaergaard (Wager & Deer, 1939; Wager, 1960), and Kiglapait intrusions (Morse, 1981). Mass balance calculations for these plutonic bodies suggest that the coexisting liquids followed a trend of iron enrichment throughout almost the entire crystallization interval, and late-stage melts are calculated to have ⩾22 wt% FeO* (Wager & Brown, 1967; Morse, 1981). Similarly, melting experiments on Skaergaard samples produced partial melts with up to 30 wt% FeO* (McBirney & Naslund, 1990). The data from these intrusions have long been used in the petrological literature to represent an extreme end-member case (Fenner trend) of tholeiitic differentiation paths, although no quenched glasses, representing unambiguous magmatic liquids, have been found with the compositions proposed to have been present in the late stages of differentiation of these plutonic bodies. The lack of erupted liquids with such iron-rich compositions may in part reflect the high densities of such magmas (Sparks *et al.*, 1980; Stolper & Walker, 1980) but an alternative, albeit contentious, proposal is that such iron-rich melts did not exist, and are an artefact of the assumptions and uncertainties inherent in the calculation of liquid compositions from plutonic rocks (Hunter & Sparks, 1987, 1990; disputed by Brooks & Nielsen, 1990; McBirney & Naslund, 1990; Morse, 1990). In this case, iron enrichment in the melt would occur at approximately constant silica content until the onset of magnetite crystallization, after which liquids would follow a trend of iron depletion and silica enrichment, similar to those seen in many volcanic provinces (e.g. Iceland; Carmichael, 1964). The experiments documented in this paper provide new information on the effects of oxygen fugacity on the saturation of magnetite and ilmenite in differentiating basaltic magmas, and thus provide some insights into the factors influencing the degree of iron enrichment that may be obtained during crystallization of initially basaltic magmas under low-pressure and anhydrous conditions.

Experimental studies of basaltic analogue systems such as SiO_2–MgO–FeO–Fe_2O_3 (Muan & Osborn, 1956), CaO–SiO_2–MgO–FeO–Fe_2O_3 (Presnall, 1966) and MgO–FeO–Fe_2O_3–$CaAl_2Si_2O_8$–SiO_2 (Roeder & Osborn, 1966) show that the phase equilibria and liquid lines of descent depend strongly on oxygen fugacity, because of its large influence on magnetite stability. The work of Osborn (1959) and Presnall (1966) indicates that iron depletion in the melt is inevitable after the onset of magnetite crystallization if crystallization takes place at fixed f_{O_2}. Greater iron enrichment is possible in systems where the oxygen fugacity is low enough to suppress magnetite crystallization, or in magnetite-saturated systems which are closed to oxygen. In the latter case, magnetite-saturated melts may show continued iron enrichment, thus providing experimental support for the calculated liquid trend of the Skaergaard. However, erroneous conclusions may be reached when comparing simple analogues with compositionally more complex natural systems. The simple ferric iron bearing systems considered above do not contain sodium, thus restricting formation of the plagioclase solid solution series, and they lack titanium, which is necessary for the formation of minerals of the magnetite–ulvöspinel (Fe_3O_4–Fe_2TiO_4), and the ilmenite–haematite ($FeTiO_3$–Fe_2O_3) solid solution series, both of which are common in evolved natural systems.

Experimental studies of natural basaltic compositions (e.g. Hill & Roeder, 1974; Grove & Baker, 1984; Juster *et al.*, 1989; Snyder *et al.*, 1993; Thy & Lofgren, 1994) provide general information on the effects of f_{O_2} on iron enrichment and Fe–Ti oxide stabilities in selected compositions at low pressures. They do not, however, consider the effects of fractional crystallization or evolution in a system closed to oxygen on basaltic differentiation paths, and they do not provide any general means of predicting when or if Mt and Ilm will crystallize. In this paper we present new experimental results on phase relations, Fe–Ti oxide stabilities, melt composition trends and mineral–melt partitioning of major elements, obtained in a series of mainly equilibrium crystallization experiments on a ferro-basaltic composition over a range of f_{O_2} from 2 log units below to 1·5 log units above the fayalite–magnetite–quartz (FMQ) buffer; this work forms part of a study designed to address whether the conclusions of Osborn (1959) and Presnall (1966) concerning the role of f_{O_2} and the effect of magnetite crystallization on liquid lines of descent in basaltic systems are applicable to complex natural systems such as those of Skaergaard or Kiglapait. Furthermore, the factors controlling the saturation surfaces of Fe–Ti oxides in natural systems are evaluated in general terms. Parameterization of the experimental results allows estimation of the liquid lines of descent for equilibrium and fractional crystallization in systems that are both open and closed to oxygen, the results of which are presented elsewhere (Toplis, 1994; Toplis & Carroll, unpublished).

EXPERIMENTAL APPROACH AND METHODS

General considerations

The chosen starting composition (SC1—see below) is an eight-component (Si–Ti–Al–Fe–Ca–Mg–Na–K oxides) synthetic ferro-basalt, corresponding in composition to a proposed parental magma for the exposed portion of the Skaergaard intrusion [basaltic dyke C of Brooks & Nielsen (1978): *mg*-number = 47 = molar MgO/(MgO+FeO) × 100]. The lack of manganese is not expected to affect the general applicability of the results, but phosphorus is known to suppress magnetite crystallization in evolved ferro-basaltic melts (and therefore favour iron enrichment of the melt phase), although it has little effect on ilmenite saturation (Toplis *et al.*, 1994). The addition of P_2O_5 is not expected to change any of the main conclusions reached in this study, although the reader is referred to Toplis *et al.* (1994) for a detailed discussion of the role of phosphorus in evolved ferro-basaltic magmas.

Experiments were carried out at atmospheric pressure, to allow careful control of oxidation state, and the results should be applicable to the differentiation of basaltic magmas at low pressures (e.g. Wager & Brown, 1967; Walker *et al.*, 1979). The small pressure differences between crustal-level natural systems and the experiments is not expected to change significantly the conclusions drawn from this study, although the lack of volatiles at 1 atm, especially H_2O, may mean that the results do not accurately reflect the phase equilibria at the most advanced stages of fractionation.

The range of studied oxygen fugacity (f_{O_2}) is important because of its influence on Fe^{3+}/Fe^{2+} ratio (Kennedy, 1948; Fudali, 1965; Sack *et al.*, 1980; Kilinc *et al.*, 1983). For a fixed composition the Fe^{3+}/Fe^{2+} ratio of the melt phase is approximately constant along T–f_{O_2} paths which parallel the FMQ solid buffer (Fudali, 1965; Sato, 1978; Carmichael & Ghiorso, 1986), and it is thus convenient to quote oxygen fugacities relative to the FMQ buffer at the temperature of interest. Our experiments were performed between one $\log_{10} f_{O_2}$ unit above, and two $\log_{10} f_{O_2}$ units below the FMQ buffer curve (FMQ+1 to FMQ−2), a range of f_{O_2} typical of that inferred from both plutonic and volcanic tholeiitic rock series (Williams, 1971; Frost *et al.*, 1988; Carmichael, 1991). Over this range of f_{O_2} the atomic $Fe^{3+}/\Sigma Fe$ of the starting composition, estimated using the calculation scheme of Kilinc *et al.* (1983), varies from ~0·21 at FMQ+1 to ~0·06 at FMQ−2.

Starting materials

The starting materials were synthetic glass powders prepared from mixtures of reagent grade oxides (SiO_2, TiO_2, Al_2O_3, Fe_2O_3, MgO) and carbonates ($CaCO_3$, Na_2CO_3, K_2CO_3). The glasses were prepared in a thin-walled platinum crucible which was pre-saturated with iron using the melt composition being synthesized. The oxide–carbonate mixtures were initially decarbonated in air for 30 min at ~800°C before complete fusion in air at ~1300°C for 4 h. This molten material was then poured into a graphite crucible and allowed to cool to room temperature before being finely crushed in an agate mortar under acetone. This powder was then remelted at ~1300°C for a further 4 h, removed and recrushed as before. Microprobe analyses of chips of the starting materials show them to be homogeneous in composition. To maintain a reasonably high liquid proportion over a large crystallization interval two starting compositions were used. Composition SC1 was used for experiments ranging from near-liquidus to ~50% crystallized. A second composition (SC4) was synthesized, corresponding to that of the residual glass composition after ~40% crystallization of SC1. The use of SC4 thus represents a fractionation event during the crystallization of SC1. Equilibrium crystallization experiments were performed using SC4 to lower temperatures, allowing the description of the liquid line of descent of SC1 from above the liquidus to ~90% crystallized.

Experimental methods

For each experiment ~100 mg of starting material was pressed onto a loop of 0·15 mm diameter platinum wire, using polyvinyl alcohol as a binder. To minimize sample iron loss, all loops were pre-saturated using the composition of interest at the required f_{O_2} for 24 h (Grove, 1981), followed by cleaning in HF before each formal experiment. Samples were suspended in the hot spot of a Gero 1-atm gas mixing furnace, with furnace temperature controlled using a Eurotherm 818 controller and measured by a $Pt_{94}Rh_6$–$Pt_{70}Rh_{30}$ thermocouple located just above the sample in the hot spot of the furnace; thermocouple calibration was checked against the melting point of gold (1064°C). Oxygen fugacity was controlled using a CO–CO_2 gas mixture (Deines *et al.*, 1974), and was measured in the hot spot of the furnace, using a yttrium-stabilized zirconia probe that was calibrated against the Ni–NiO reaction (Huebner & Sato, 1970). Gas flow rates were maintained at ~300 cm^3/min, corresponding to a linear flow rate of 3 mm/s for the 4·5 cm diameter furnace tube, shown to be sufficient to

fix f_{O_2} while minimizing Na_2O loss (Tormey *et al.*, 1987).

The experimental charges were initially held above their liquidus for a duration D_1 (typically 9 h) to allow redox equilibration of the melt, then cooled at a constant rate to the final temperature of interest. Samples were left at the final temperature for a duration D_2 to allow equilibration between crystalline phases and coexisting melts. Details of the experimental conditions, cooling history and resulting phase assemblage for each experiment are summarized in Table 1. Samples were drop-quenched into water by fusing a fine Pt suspension wire, and polished sections of the quenched charges were made for petrographic and electron probe analysis.

Analysis

The electron-microprobe analyses were performed using a JEOL JXA 8600 electron microprobe at the University of Bristol, operated at an accelerating voltage of 15 kV and 15 nA beam current. Counting times were 30 s on peak and background during standardization, and 15 s during analyses. Standards used were albite for Na and Al, St Johns Island olivine for Mg, wollastonite for Si and Ca, adularia for K, Fe_2O_3 for Fe and $SrTiO_3$ for Ti, and data were reduced by the ZAF method. The ferro-basaltic glass from the super-liquidus experiment Fe-20 (see Table 2) was analysed during each session to ensure compatibility between analyses obtained over the course of the study. Incident-beam diameter was 10 μm on glass and 5 μm on plagioclase to minimize potential Na_2O volatility under the electron beam. A focused beam was used on all other phases. The electron probe analyses of all the glass and crystalline phases in each experiment are presented in Table 2.

Compositional changes and attainment of equilibrium

Despite the efforts made to minimize sodium loss to the gas stream, and iron exchange between the sample and platinum loop, some changes in sample bulk composition are inevitable. Their magnitudes have been estimated from the residuals of mass balance calculations using a weighted multiple least-squares regression of the data presented in Table 2. The minimization procedure of Albarède & Provost (1977) incorporated into a program written by M. Baker was used to perform this. The calculations indicate that iron loss (or gain) is generally less than $\pm 5\%$ relative, and that sodium loss is typically $\sim 6\%$ (relative), going as high as $\sim 12\%$ (relative) in the longer duration runs. Table 3 shows the calculated weight proportions of phases, estimated sodium loss, and regression statistics.

To facilitate a close approach to equilibrium in our experiments we attempted to limit experiments to conditions where the melt fraction was $>30\%$, and longer run durations in lower-temperature experiments were used (see Table 1). The run products consist of euhedral crystalline phases homogeneously distributed throughout the charge, and backscattered electron images of the experimental charges (Figs 1a–d) show their composition to be approximately homogeneous. This is confirmed by the standard deviations of multiple electron probe analyses of each phase (Table 2). Glass, olivine, magnetite and ilmenite, irrespective of location within the sample, show constant compositions within the counting statistics of the microprobe analyses. Clinopyroxene and plagioclase were observed to have greater ranges of composition owing to the slower diffusion rates, and consequently longer equilibration times, for these phases. In a single charge total variations are typically ± 3 mol % An for plagioclase, and ± 3 mol % Wo, En, Fs for high-calcium pyroxene, although rim compositions more typically show variations of ± 1 mol % An, and ± 2 mol % Wo, En, Fs. Zoning was most evident in low-temperature experiments using SC1 along the FMQ buffer, as noted in Table 2. Despite these minor inhomogeneities, evidence of close approach to equilibrium is provided by the partitioning of elements between crystals and coexisting melts, e.g. $K_{dFe\text{-}Mg}^{Ol\text{-}Liq}$ (Roeder & Emslie, 1970), and $D_{CaO}^{Ol\text{-}Liq}$ (Jurewicz & Watson, 1988). Our experimental results are in broad agreement with the above, although the effects of low *mg*-number on these distribution coefficients will be discussed in more detail below. Two reversal experiments were also done, in which the charges were melted, crystallized, and then heated to their final temperature. These were at 1115°C at FMQ using SC1, and at 1072°C at FMQ − 1 using SC4. Details of the cooling paths for these two experiments are given in Table 1. The resulting phase relations, and mineral and liquid compositions are in excellent agreement with those obtained by direct cooling, further supporting the view that equilibrium was closely approached.

RESULTS

Phase equilibria

The phase relations of composition SC1, and its residual, fractionated liquid SC4 are shown in temperature–oxygen fugacity space in Fig. 2; the five crystalline phases observed are olivine (Ol), plagioclase (Plag), Ca-rich clinopyroxene (Cpx),

Table 1: Cooling history, run conditions, and run products

Run no.[a]	Cooling history			Final conditions			Run products[f]
	$D1$[b] (h)	Ramp (°C/h)	D_2[c] (h)	T_f[d] (°C)	$\log_{10}f_{O_2}$	ΔFMQ[e]	
Super-liquidus							
Fe-20	—	—	6	1166	−8·92	−0·10	Gl
Fe-18	—	—	14	1170	−10·57	−1·80	Gl
Fe-48*	—	—	25	1126	−10·67	−1·34	Gl
Fe-50†	—	—	41	1123	−9·23	+0·13	Gl
'FMQ + 1'							
Fe-40	10	3	47	1146	−8·05	+1·02	Gl, Ol, Pl
Fe-79	27	3	71	1130	−8·32	+0·95	Gl, Ol, Pl, Cpx
Fe-41	10	3	140	1122	−8·08	+1·35	Gl, Ol, Pl, Cpx, Mt
Fe-95*	9	3	263	1072	−9·16	+0·89	Gl, Pl, Cpx, Mt, Ilm
'FMQ'							
Fe-45	12	5	47	1158	−8·95	−0·03	Gl, Ol, Pl
Fe-36	10	3	28	1134	−9·19	+0·03	Gl, Ol, Pl
Fe-37	10	3	89	1125	−9·55	−0·21	Gl, Ol, Pl, Cpx
Fe-35	8	5	143	1125	−9·36	−0·02	Gl, Ol, Pl, Cpx
Fe-39	10	3	243	1115	−9·48	−0·01	Gl, Ol, Pl, Cpx
Fe-44R[g]	8	5/2[g]	290	1115	−9·41	+0·06	Gl, Ol, Pl, Cpx
Fe-42	5	10	198	1105	−9·56	+0·04	Gl, Ol, Pl, Cpx
Fe-43	12	2	115	1096	−9·74	−0·02	Gl, Ol, Pl, Cpx, Mt, Ilm
Fe-21	5	20	255	1095	−10·01	−0·27	Gl, Ol, Pl, Cpx, Mt, Ilm
Fe-47*	10	3	127	1087	−9·87	−0·03	Gl, Pl, Cpx, Mt, Ilm
Fe-51†	10	3	273	1078	−9·96	+0·00	Gl, Pl, Cpx, Mt, Ilm
Fe-49*	10	3	247	1068	−10·11	+0·00	Gl, Pl, Cpx, Mt, Ilm
Fe-52†	10	3	250	1057	−10·32	−0·06	Gl, Pl, Cpx, Mt, Ilm
'FMQ − 1'							
Fe-24	5	10	15	1147	−10·08	−1·02	Gl, Ol, Pl
Fe-23	5	10	26	1126	−10·25	−0·92	Gl, Ol, Pl, Cpx
Fe-25	5	10	49	1110	−10·74	−1·20	Gl, Ol, Pl, Cpx
Fe-67†	9	3	175	1102	−10·66	−1·02	Gl, Ol, Pl, Cpx, Ilm
Fe-68†	9	3	192	1093	−10·77	−1·01	Gl, Ol, Pl, Cpx, Ilm

(continued on next page)

Table 1: continued

Run no.[a]	Cooling history			Final conditions			Run products[f]
	$D1$[b] (h)	Ramp (°C/h)	D_2[c] (h)	T_f[d] (°C)	$\log_{10} f_{O_2}$	ΔFMQ[e]	
Fe-71*	9	3	285	1081	−10·92	−1·00	Gl, Ol, Pl, Cpx, Ilm
Fe-77*	9	3	184	1073	−11·31	−1·28	Gl, Ol, Pl, Cpx, Ilm
Fe-126*R[h]	9	−3[h]	262	1072	−11·15	−1·10	Gl, Ol, Pl, Cpx, Ilm
Fe-136*	9	3	215	1072	−10·79	−0·74	Gl, Ol, Pl, Cpx, Mt, Ilm
Fe-70*	9	3	278	1061	−11·21	−1·01	Gl, Ol, Pl, Cpx, Mt, Ilm
'FMQ−2'							
Fe-16	4	20	39	1148	−10·89	−1·85	Gl, Ol, Pl
Fe-15	4	20	52	1118	−11·30	−1·87	Gl, Ol, Pl
Fe-56	10	3	316	1111	−11·62	−2·10	Gl, Ol, Pl, Cpx
Fe-62	10	3	247	1098	−11·81	−2·12	Gl, Ol, Pl, Cpx, Ilm
Fe-63†	10	3	247	1098	−11·81	−2·12	Gl, Ol, Pl, Cpx
Fe-19	5	30	159	1095	−11·66	−1·92	Gl, Ol, Pl, Cpx, Ilm
Fe-66†	10	3	189	1090	−11·79	−1·99	Gl, Ol, Pl, Cpx, Ilm
Fe-65†	10	3	167	1079	−11·97	−2·02	Gl, Ol, Pl, Cpx, Ilm
Fe-59†	10	3	269	1071	−12·26	−2·20	Gl, Ol, Pl, Cpx, Ilm
Fe-61†	10	3	208	1059	−12·44	−2·21	Gl, Ol, Pl, Cpx, Ilm
Fe-76†	9	3	514	1050	−12·35	−1·99	Gl, Ol, Pl, Cpx, Ilm

[a] The experimental runs are divided into groups of experiments carried out at conditions approximately parallel to the FMQ buffer and listed in order of decreasing temperature within each group. The starting composition used is SC1 unless marked by * which signifies the use of SC4, or † which signifies the use of SC4a, a second synthesis of SC4. Exact compositions are given in Table 2. R represents reversal experiments (see notes g and h below).
[b] D_1 represents the dwell above the liquidus to allow the equilibration of the iron redox ratio, before cooling.
[c] D_2 represents the dwell at the final temperature of interest, to allow liquid–solid reactions to take place.
[d] T_f represents the final temperature of the experiment.
[e] ΔFMQ represents $\log f_{O_2}$ (experiment) − $\log f_{O_2}$ (FMQ buffer), as estimated from data for fayalite ⇌ magnetite + quartz solid reaction by O'Neill (1987).
[f] Abbreviations used are: Gl, glass; Ol, olivine; Pl, plagioclase; Cpx, calcium-rich clinopyroxene; Mt, magnetite–ulvöspinel solid solution; Ilm, ilmenite–haematite solid solution.
[g] A 'reversal' experiment using SC1. The charge was held above its liquidus for 8 h, cooled at 5°C/h to 1050°C where it was left for 17 h, heated at 5°C/h to 1100°C, then left for 2 h before heating at 2°C/h to the final temperature of 1115°C.
[h] A 'reversal' experiment using SC4. The charge was held above its liquidus for 9 h, quenched and returned to the furnace at 1040°C for 9 h before heating at a rate of 3°C/h to the final temperature of 1072°C.

magnetite–ulvöspinel solid solution (Mt), and ilmenite–haematite solid solution (Ilm). The liquidus of SC1 lies between 1166°C and 1158°C, where olivine and plagioclase begin to crystallize. Plagioclase remains a stable liquidus phase throughout the studied T–f_{O_2} space, whereas olivine was absent in experiments using SC4 at or above the FMQ buffer, although it was observed at lower f_{O_2}. High-calcium pyroxene is the third phase to crystallize at all f_{O_2}, but its liquidus varies approximately linearly with f_{O_2}, from ~1110°C at FMQ−2, to ~1130°C at FMQ+1. Fe–Ti oxide crystallization occurs after the appearance of Cpx for all the studied conditions, but the stabilities of Mt and Ilm depend strongly on oxygen fugacity. Above the FMQ buffer magnetite is the fourth crystalline phase, followed at lower

Table 2: Electron microprobe analyses (wt %) of run products

Run no.[a]	Ph[b]	*n*[c]	SiO_2	TiO_2	Al_2O_3	FeO*	MgO	CaO	Na_2O	K_2O	Total	*X*Ph[d]
Starting compositions												
SC1	Liq	13	48·8 (3)e	2·9 (1)	14·9 (2)	13·1 (5)	6·5 (1)	10·9 (1)	2·7 (1)	0·30 (2)	100·10	46·9
SC4	Liq	11	49·5 (5)	4·3 (2)	11·5 (1)	14·6 (4)	4·8 (1)	10·0 (1)	2·9 (1)	0·48 (3)	98·08	37·0
SC4a	Liq	6	48·7 (4)	4·3 (2)	11·5 (2)	16·2 (3)	4·6 (1)	9·7 (1)	3·0 (1)	0·49 (1)	98·49	33·6
'FMQ + 1'												
Fe-40	Liq	9	48·3(3)	3·30(14)	12·6(1)	14·20(28)	5·83(6)	10·60(8)	2·61(8)	0·33(3)	97·77	48·0
	Ol	6	39·10(28)	0·06(3)	0·05(3)	21·90(32)	38·10(34)	0·46(4)	0·03(2)	0·0(0)	99 70	75·6
	Plag	8	49·84(15)	0·18(3)	29·57(21)	2·30(28)	0·40(6)	14·61(17)	2·99(7)	0·12(1)	100·01	72·5
Fe-79	Liq	12	48·17(37)	4·20(11)	11·80(11)	15·73(21)	5·17(7)	10·56(7)	2·57(6)	0·55(2)	98·75	42·6
	Ol	12	37·83(35)	0·10(4)	0·08(3)	27·81(35)	34·53(40)	0·51(3)	0 06(2)	0·0(0)	100·92	68·9
	Plag	8	52·18(41)	0·16(3)	29·26(25)	1·38(10)	0·28(5)	13·26(23)	3·71(15)	0·16(2)	100·39	65·8
	Cpx	8	49·71(52)	1·96(24)	3·73(28)	10·94(55)	14·23(45)	19·75(70)	0·32(2)	0·0(0)	100·64	69·9
Fe-41	Liq	12	49·2(4)	3·70(16)	11·72(18)	15·20(32)	4·85(7)	9·62(7)	2·90(8)	0·57(3)	97·76	42·0
	Ol	6	37·94(35)	0·13(5)	0·01(1)	25·34(36)	34·51(20)	0·51(6)	0·05(4)	0·0(0)	98·49	70·8
	Plag	9	51·27(95)	0·20(8)	29·15(41)	2·13(36)	0·34(9)	14·01(54)	3·55(31)	0·16(2)	100·81	67·9
	Cpx	10	50·14(22)	1·56(5)	3·40(7)	10·61(46)	14·85(16)	20·06(43)	0·35(3)	0·0(0)	100·97	71·4
	Mt	7	0·55(2)	15·81(19)	3·98(5)	69·50(39)	4·74(3)	0·53(17)	0·03(2)	0·0(0)	95·14	31·9
Fe-95*	Liq	9	62·29(73)	2·52(17)	11·90(17)	9·34(32)	1·44(6)	5·22(26)	3·26(26)	1·53(7)	97·55	25·2
	Plag	13	54·19(70)	0·18(6)	27·26(26)	1·18(12)	0·11(2)	11·46(29)	4·82(18)	0·17(4)	99·40	56·2
	Cpx	11	48·97(98)	1·95(40)	2·18(47)	14·03(99)	12·63(88)	18·85(92)	0·32(2)	0·01(1)	98·96	61·6
	Mt	7	0·11(4)	20·69(28)	1·88(8)	69·81(85)	2·36(6)	0·16(6)	0·02(2)	0·01(1)	95·04	30·5
	Ilm	9	0·05(3)	47·28(57)	0·29(4)	46·29(38)	2·96(12)	0·24(8)	0·02(3)	0·02(2)	97·15	90·1

(continued on next page)

Table 2: continued

Run no.[a]	Ph[b]	*n*[c]	SiO_2	TiO_2	Al_2O_3	FeO*	MgO	CaO	Na_2O	K_2O	Total	*X*Ph[d]
'FMQ'												
Fe-45	Liq	19	48·5(3)	3·25(17)	13·79(9)	13·59(30)	6·5(1)	10·50(8)	2·55(7)	0·32(3)	99·00	49·5
	Ol	8	39·00(19)	0·02(3)	0·0(0)	23·2(3)	37·8(3)	0·35(2)	0·01(1)	0·0(0)	100·38	74·4
	Plag	20	51·58(40)	0·15(6)	30·67(42)	0·67(8)	0·15(2)	14·26(31)	3·23(19)	0·0(0)	100·71	70·9
Fe-36	Liq	11	49·2(5)	3·80(29)	12·32(12)	14·79(50)	5·46(15)	10·90(6)	2·7(1)	0·43(4)	99·60	43·4
	Ol	9	38·50(19)	0·06(7)	0·0(0)	26·40(29)	35·30(19)	0·47(3)	0·01(1)	0·0(0)	100·74	70·5
	Plag	16	52·09(84)	0·08(6)	30·73(61)	1·18(29)	0·23(11)	14·22(49)	3·28(33)	0·0(0)	101·81	70·6
Fe-37	Liq	12	49·0(4)	4·10(29)	11·82(16)	15·18(40)	5·18(15)	10·90(12)	2·60(9)	0·47(3)	99·25	41·1
	Ol	7	37·90(29)	0·13(3)	0·0(0)	28·30(49)	34·00(28)	0·55(2)	0·05(1)	0·01(1)	100·94	68·2
	Plag	11	51·48(68)	0·23(13)	30·08(67)	1·61(33)	0·41(15)	14·56(55)	3·10(30)	0·12(2)	101·59	71·7
	Cpx	2	51·42	1·48	3·33	9·15	14·32	20·47	0·28	0·00	100·45	73·6
Fe-35	Liq	13	48·6(5)	4·35(20)	11·82(13)	15·06(30)	5·03(12)	10·6(6)	2·63(8)	0·47(4)	98·56	40·9
	Ol	8	38·40(19)	0·08(5)	0·06(4)	27·7(3)	33·7(2)	0·56(3)	0·02(2)	0·0(0)	100·52	68·4
	Plag	12	53·28(57)	0·15(7)	29·15(30)	1·62(33)	0·41(14)	13·70(31)	3·57(29)	0·13(1)	102·01	67·4
	Cpx	14	51·5(5)	1·6(2)	3·5(4)	9·2(4)	14·3(3)	20·5(6)	0·28(4)	0·0(0)	100·88	73·5
Fe-39	Liq	16	49·0(7)	4·62(20)	11·68(16)	15·74(30)	4·69(17)	9·71(9)	2·79(9)	0·58(4)	98·81	38·2
	Ol	6	37·80(27)	0·08(5)	0·01(2)	29·80(16)	32·00(11)	0·50(1)	0·01(1)	0·0(0)	100·20	65·7
	Plag	8	53·57(47)	0·11(6)	29·53(32)	1·40(28)	0·19(4)	13·17(35)	4·10(18)	0·02(1)	101·98	64·5
	Plag‡	18	52·5(7)	0·20(9)	29·3(5)	1·90(45)	0·40(18)	14·2(8)	3·40(55)	0·03(2)	101·93	
	Cpx	10	51·20(99)	1·70(38)	3·20(56)	9·80(28)	14·10(68)	20·10(38)	0·28(4)	0·0(0)	100·38	72·0

Fe-44R	Liq	17	48·3(3)	4·45(30)	11·58(11)	16·03(40)	4·71(12)	9·80(7)	2·73(10)	0·53(4)	98·13	38·0
	Ol	11	37·60(9)	0·10(6)	0·0(0)	30·40(47)	31·70(8)	0·46(1)	0·01(1)	0·0(0)	100·27	65·0
	Plag	13	53·76(68)	0·21(7)	28·56(40)	1·24(18)	0·19(3)	12·70(35)	4·02(20)	0·03(1)	100·71	63·5
	Plag‡	25	52·26(118)	0·21(8)	29·10(65)	1·62(42)	0·28(12)	13·72(85)	3·41(58)	0·03(2)	100·63	
	Cpx	16	51·5(5)	1·40(19)	2·6(3)	10·30(47)	14·49(41)	19·51(68)	0·27(2)	0·0(0)	100·07	71·5
Fe-42	Liq	8	48·7(5)	5·10(19)	11·15(19)	16·3(5)	4·23(17)	9·30(8)	2·90(11)	0·57(5)	98·25	35·1
	Ol	13	36·77(18)	0·16(4)	0·03(1)	32·41(31)	29·93(21)	0·47(3)	0·0(0)	0·0(0)	99·77	62·2
	Plag	9	53·20(59)	0·37(21)	27·90(66)	1·63(49)	0·28(16)	12 57(31)	3·97(21)	0·0(0)	99·92	63 6
	Plag‡	20	51·97(94)	0·39(24)	28·38(86)	2·09(55)	0·36(18)	13·48(80)	3·45(45)	0·0(0)	100·12	
	Cpx	11	50·30(94)	1·98(44)	2·81(80)	10·79(55)	13·68(41)	19·65(61)	0·28(5)	0·0(0)	99·49	69·3
Fe-43	Liq	16	49·49(50)	4·65(40)	11·28(18)	16·72(50)	3·86(20)	8·60(11)	3·03(9)	0·78(7)	98·41	32·4
	Ol	13	36·78(15)	0·08(4)	0·0(0)	35·84(32)	27·54(24)	0·48(2)	0·01(1)	0·0(0)	100·73	57·8
	Plag	8	54·20(68)	0·3(2)	26·70(76)	1·80(32)	0·40(13)	12·00(77)	4 20(28)	0·11(6)	99·71	60·8
	Plag‡	19	52·96(110)	0·30(16)	27·36(85)	2·18(42)	0·40(18)	12·99(94)	3·70(45)	0·08(6)	99·97	
	Cpx	10	51·77(42)	1·24(17)	2·05(31)	12·67(51)	14·76(49)	17·43(84)	0·28(3)	0·0(0)	100·20	67·5
	Mt	12	0·14(4)	22·15(49)	3·24(15)	67·12(50)	3·79(17)	0·44(7)	0·07(4)	0·01(1)	96·96	23·2
	Ilm	5	0·04(3)	48·83(45)	0·47(6)	42·95(52)	5·08(12)	0·35(5)	0·0(0)	0·0(0)	97·72	91·3
Fe-21	Liq	9	49·01(85)	4·55(36)	11·59(9)	17·46(71)	4·23(25)	8·72(23)	2·95(8)	0·83(4)	99·34	33·1
	Ol	5	36·76(49)	0·14(10)	0·03(2)	34·58(84)	28·25(16)	0·47(2)	0·01(1)	0·0(0)	100·24	59·3
	Plag	8	54·95(85)	0·23(5)	28·25(39)	1·23(17)	0·20(3)	12·20(44)	4·35(27)	0·26(4)	101·67	59·9
	Plag‡	25	53·21(160)	0·21(5)	29·18(84)	1·60(38)	0·25(5)	13·83(120)	3·6(7)	0·18(8)	102·06	
	Cpx	9	52·78(79)	1·13(16)	2·02(31)	13·37(56)	15·18(43)	16·32(76)	0·26(2)	0·01(1)	101·07	66·9
	Mt	11	0·12(4)	24·51(50)	3·13(15)	64·21(47)	4·17(11)	0·47(7)	0·11(6)	0·02(1)	96·74	18·1
	Ilm	5	0·02(2)	49·01(38)	0·46(5)	42·31(59)	5·39(14)	0·57(8)	0·0(0)	0·0(0)	97·76	91·3

(continued on next page)

Table 2: continued

Run no.[a]	Ph[b]	*n*[c]	SiO_2	TiO_2	Al_2O_3	FeO*	MgO	CaO	Na_2O	K_2O	Total	*X*Ph[d]
Fe-47*	Liq	19	50·6(4)	4·60(21)	10·85(15)	16·98(40)	3·39(13)	8·20(8)	3·23(9)	0·74(4)	98·59	29·3
	Plag	20	55·94(68)	0·21(9)	27·25(22)	0·99(11)	0·09(3)	10·73(18)	5·15(12)	0·0(0)	100·36	53·5
	Cpx	12	50·74(65)	1·61(34)	2·28(50)	13·25(44)	14·01(43)	17·40(65)	0·27(3)	0·0(0)	99·56	65·3
	Mt	12	0·02(2)	24·15(23)	2·51(8)	66·17(53)	3·35(7)	0·16(5)	0·09(2)	0·0(0)	96·45	21·0
	Ilm	9	0·0(0)	49·38(34)	0·46(4)	44·11(25)	3·99(7)	0·23(4)	0·08(3)	0·02(1)	98·27	92·2
Fe-51†	Liq	14	54·45(30)	3·29(15)	11·18(9)	15·15(16)	2·54(13)	7 00(5)	3·41(8)	1·07(3)	98·09	25 8
	Plag	20	57·08(21)	0·14(8)	26·27(44)	1·10(29)	0·13(4)	10·04(16)	5·48(8)	0·25(2)	100·49	49·6
	Cpx	12	50·98(47)	1·25(50)	1·69(18)	14·95(34)	13·03(44)	17·60(78)	0·25(2)	0·0(0)	99·75	60·8
	Mt	13	0·10(8)	23·86(29)	2·18(5)	67·49(46)	2·70(7)	0·24(6)	0·06(4)	0·02(1)	96·65	22·6
	Ilm	12	0·04(4)	48·41(25)	0·46(5)	44·94(23)	3·36(7)	0·30(6)	0·07(2)	0·02(1)	97·60	91·5
Fe-49*	Liq	13	59·5(4)	2·40(21)	11·96(10)	12 81(30)	1·89(12)	5·70(7)	3·52(10)	1·54(5)	99·32	23·3
	Plag	25	56·62(80)	0·08(7)	26·66(30)	0·94(30)	0·08(1)	10·26(40)	5·16(15)	0·28(2)	100·08	51·5
	Cpx	13	50·12(48)	1·38(24)	1·80(24)	16·35(66)	11·45(53)	18·05(79)	0·25(3)	0·02(1)	99·42	55·5
	Mt	14	0·09(5)	22·95(49)	2·15(10)	68·35(43)	2·35(7)	0·30(9)	0·05(3)	0·01(1)	96·25	24·8
	Ilm	5	0·07(3)	47·19(64)	0·50(9)	45·18(39)	3·07(9)	0·50(8)	0·07(3)	0·01(1)	96·59	90·4
Fe-52†	Liq	15	64·27(40)	2·03(11)	12·08(12)	9·58(30)	1·23(9)	4·31(2)	3·55(7)	1·85(4)	98·90	20·7
	Plag	21	58·60(48)	0·13(5)	25·70(28)	0·96(3)	0·08(1)	8·90(18)	6·10(22)	0·33(2)	100·80	43·8
	Cpx	12	49 76(93)	1·63(42)	1·94(61)	16·66(78)	10·91(76)	18·30(78)	0·31(3)	0·01(1)	99·52	53·8
	Mt	14	0·17(7)	24·24(41)	1·88(9)	67·29(51)	2·09(9)	0·32(8)	0·07(2)	0·02(1)	96·08	22·2
	Ilm	5	0·02(1)	47·90(54)	0·43(7)	46·20(35)	2·51(8)	0·30(5)	0·0(0)	0·0(0)	97·36	91·6
'FMQ-1'												
Fe-24	Liq	10	48·30(67)	3·20(12)	13·30(14)	13 69(59)	6·00(19)	10·70(21)	2·71(11)	0·37(8)	98·26	46·1

	Ol	4	38·49(20)	0·10(6)	0·05(1)	25·01(38)	36·1(3)	0·45(2)	0·01(1)	0·0(0)	100·21	72·0
	Plag	9	51·18(51)	0·13(6)	30·32(37)	1·40(30)	0·40(12)	14·9(6)	3·0(3)	0·10(3)	101·43	72·9
Fe-23	Liq	12	48·40(38)	4·40(28)	12·12(11)	14·87(39)	4·93(5)	10·80(15)	2·66(7)	0·59(7)	98·77	39·5
	Ol	7	38·49(29)	0·12(5)	0·06(3)	27·89(84)	33·41(65)	0·58(11)	0·04(5)	0·0(0)	100·59	68·1
	Plag	16	52·50(38)	0·17(6)	30·84(36)	0·85(9)	0·21(1)	14·25(37)	3·27(19)	0·19(3)	102·28	69·9
	Cpx	11	50·62(38)	2·19(31)	4·01(28)	8·69(32)	13·70(23)	20·89(21)	0·29(2)	0·01(1)	100·40	73·7
Fe-25	Liq	9	48·07(55)	5·16(26)	11·23(20)	16·33(45)	4·27(9)	9·93(17)	2·78(15)	0·62(5)	98·40	33·7
	Ol	10	37·20(18)	0·24(7)	0·01(1)	32·6(4)	29·90(41)	0·58(5)	0·05(1)	0·01(1)	100·59	62·1
	Plag	14	53·01(46)	0·24(8)	29·83(52)	1·11(11)	0·26(5)	13·61(36)	3·59(30)	0·15(2)	101·80	67·1
	Cpx	14	50·41(76)	2·57(44)	3·48(52)	10·21(37)	13·16(41)	20·36(34)	0·30(3)	0·0(0)	100 49	69·7
Fe-67†	Liq	10	49·41(35)	4·90(21)	10·56(8)	17·28(32)	3·41(9)	8·65(7)	2·98(10)	0·77(4)	97·96	27·9
	Ol	11	34·61(18)	0·17(5)	0·03(1)	39·26(46)	24·77(23)	0·54(2)	0·03(1)	0·0(0)	99·41	52·9
	Plag	20	54·10(35)	0·25(6)	27·10 (52)	1·45(55)	0·26(8)	11·20(22)	4·80(16)	0·20(3)	99·36	55·7
	Cpx	14	49·80(68)	1·43(19)	2·55(56)	12·04(86)	13·37(38)	20·10(65)	0·31(7)	0·02(2)	99·62	66·4
	Ilm	10	0·29(2)	50·60(30)	0·29(2)	41·50(32)	4·19(9)	0·30(9)	0·04(2)	0·03(1)	97·24	96·1
Fe-68†	Liq	17	50·32(52)	4·40(17)	10·70(16)	18·45(38)	2·97(9)	8·38(17)	3·17(8)	0·88(6)	99·27	24·0
	Ol	13	34·59(16)	0·17(7)	0·02(2)	43·21(51)	22·20(25)	0·56(4)	0·02(2)	0·01(1)	100·78	47·8
	Plag	19	55·35(62)	0·24(6)	27·62(66)	1·19(23)	0·15(3)	10·92(41)	5·07(18)	0·24(3)	100·78	53·6
	Cpx	16	50·36(31)	1·27(16)	1·39(27)	15·61(40)	12·39(18)	18·60(24)	0·28(5)	0·02(1)	99·92	58·6
	Ilm	9	0·25(6)	51·48(56)	0·25(6)	43·08(57)	3·75(12)	0·38(7)	0·02(3)	0·01(1)	99·22	96·1

(continued on next page)

Table 2: continued

Run no.[a]	Ph[b]	n[c]	SiO_2	TiO_2	Al_2O_3	FeO*	MgO	CaO	Na_2O	K_2O	Total	XPh[d]
Fe-71*	Liq	15	52·34(47)	3·70(21)	10·70(11)	18·07(32)	2·41(5)	7·67(15)	3·28(6)	1·07(6)	99·25	20·8
	Ol	11	33·62(19)	0·38(20)	0·04(3)	48·61(36)	17·23(21)	0·64(6)	0·11(8)	0·01(1)	100·64	38·7
	Plag	19	55·78(98)	0·20(4)	27·46(78)	0·98(19)	0·09(3)	10·39(77)	5·49(40)	0·27(5)	100·66	50·3
	Cpx	15	50·54(44)	1·26(25)	1·55(42)	17·39(58)	11·51(52)	17·65(59)	0·39(7)	0·02(2)	100·31	54·1
	Ilm	6	0·25(5)	50·41(25)	0·27(3)	44·03(27)	2·76(13)	0·39(3)	0·25(11)	0·02(1)	98·38	94·8
Fe-77*	Liq	18	52·90(46)	3·49(8)	11·08(13)	17·24(40)	2·27(6)	6·95(13)	3·35(9)	1·20(6)	98·48	20·4
	Ol	8	33·25(13)	0·13(4)	0·01(1)	48·41(47)	17·86(20)	0·56(5)	0·02(2)	0·01(1)	100·25	39·7
	Plag	15	55·31(87)	0·21(4)	27·15(63)	0·98(12)	0·11(2)	10·07(66)	5·49(36)	0·28(5)	99·60	49·5
	Cpx	12	49·40(65)	1·80(45)	1·91(42)	16·25(64)	11·98(37)	17·76(53)	0·25(4)	0·01(1)	99·36	56·8
	Ilm	8	0·06(4)	51·27(27)	0·21(2)	44·13(35)	2·94(12)	0·30(7)	0·01(1)	0·01(1)	98·93	96·2
Fe-126*R	Liq	4	51·74(16)	3·55(14)	10·43(49)	17·25(19)	2·30(9)	7·47(4)	2·48(6)	1·18(4)	96·45	21·7
	Ol	3	33·57(17)	0·18(6)	0·24(38)	45·97(33)	18·31(8)	0·64(11)	0·08(14)	0·0(0)	99·03	41·5
	Plag	4	55·63(31)	0·15(8)	25·54(26)	0·94(5)	0·09(3)	10·00(29)	5·32(22)	0·36(2)	98·10	49·9
	Cpx	6	48·94(49)	1·30(22)	1·40(28)	17·29(72)	11·72(25)	17·30(60)	0·21(4)	0·01(1)	98·23	54·7
	Ilm	5	0·24(40)	52·60(74)	0·25(9)	43·52(78)	2·90(8)	0·40(13)	0·02(2)	0·03(2)	99·95	98·2
Fe-136*	Liq	10	53·43(45)	3·22(12)	10·69(14)	17·44(66)	2·11(7)	6·92(17)	3·31(11)	1·18(6)	98·36	19·0
	Ol	8	33·20(22)	0·12(6)	0·01(2)	48·14(51)	17·53(28)	0·54(6)	0·01(2)	0·01(2)	99·58	39·4
	Plag	14	56·05(94)	0·17(6)	25·39(54)	0·90(22)	0·10(3)	10·06(78)	5·51(34)	0·37(5)	99·87	49·9
	Cpx	15	50·06(74)	1·48(46)	1·76(63)	16·07(80)	11·67(52)	18·14(65)	0·23(4)	0·02(2)	99·47	56·4
	Mt	8	0·10(4)	26·82(44)	2·01(7)	65·12(97)	2·32(9)	0·30(14)	0·01(2)	0·00(1)	96·71	15·4
	Ilm	8	0·06(9)	50·71(47)	0·20(3)	44·85(70)	2·76(6)	0·22(5)	0·01(1)	0·01(1)	98·82	95·4

JOURNAL OF PETROLOGY VOLUME 36 NUMBER 5 OCTOBER 1995

Fe-70*	Liq	16	56·19(20)	2·80(16)	11·10(10)	16·54(28)	1·70(4)	6·36(12)	3·64(8)	1·53(4)	99·86	16·8
	Ol	11	32·95(19)	0·16(5)	0·04(3)	52·39(76)	14·50(27)	0·61(5)	0·06(3)	0·01(1)	100·72	33·0
	Plag	12	57·12(74)	0·17(3)	26·64(58)	1·14(20)	0·09(4)	9·66(51)	5·84(26)	0·33(4)	100·99	46·9
	Cpx	15	50·32(41)	1·22(19)	1·37(33)	19·01(90)	10·65(51)	17·55(76)	0·31(4)	0·02(1)	100·45	50·0
	Mt	9	0·11(2)	27·84(24)	1·78(4)	66·08(55)	1·76(2)	0·29(7)	0·09(4)	0·02(1)	97·97	14·9
	Ilm	10	0·19(5)	50·71(38)	0·21(3)	45·52(41)	2·20(6)	0·28(7)	0·09(5)	0·02(1)	99·22	95·4
'FMQ – 2'												
Fe-16	Liq	11	49 80(58)	3·47(19)	13·15(16)	14·18(39)	6·06(16)	10·81(21)	2·53(15)	0·37(5)	100·37	44·7
	Ol	7	39·30(15)	0·11(6)	0·07(2)	25·20(40)	36·80(28)	0·39(4)	0·02(1)	0·0(0)	101·89	72·3
	Plag	17	51·88(37)	0·11(5)	30·58(20)	0·87(18)	0·24(4)	14·37(21)	3·24(12)	0·10(1)	101·39	70·6
Fe-15	Liq	19	49·91(48)	4·65(22)	11·63(9)	15·16(42)	4·90(10)	11·18(19)	2·54(11)	0·43(4)	100·40	38·0
	Ol	11	38·15(34)	0·16(8)	0·04(3)	29·65(41)	31·66(31)	0·58(2)	0·0(0)	0·0(0)	100·24	65·6
	Plag	19	52·85(55)	0·23(6)	29·27(35)	0·88(8)	0·25(4)	13·63(38)	3·73(19)	0·15(2)	100·99	66·3
Fe-56	Liq	12	50·53(32)	4·92(19)	11·35(12)	15·73(33)	4·08(9)	9·17(7)	2·46(7)	0·65(2)	98·89	32·8
	Ol	8	36·23(21)	0·10(1)	0·01(1)	36·23(42)	27·73(21)	0·49(1)	0 0(0)	0·01(1)	100·80	57·7
	Plag	13	53·39(41)	0 18(6)	29·13(39)	1·13(21)	0·25(6)	13·07(30)	3·82(23)	0·10(3)	101·07	65·0
	Cpx	15	51·41(46)	1·39(18)	1·70(37)	11·71(65)	14·50(36)	18·89(90)	0·18(4)	0·01(1)	99·79	68·8
Fe-62	Liq	12	50·42(30)	5·21(17)	11·05(10)	16·94(41)	3·80(8)	8·98(10)	2·69(8)	0·83(4)	99·94	29·7
	Ol	10	35·70(19)	0·12(6)	0·0(0)	37·91(19)	27·09(16)	0 53(3)	0·0(0)	0·01(1)	101·37	56·0
	Plag	13	53·23(68)	0·10(3)	29·67(57)	0·70(11)	0·12(2)	12·83(47)	4·20(17)	0·21(2)	101·06	62·0
	Cpx	17	50·32(66)	2·13(28)	2·62(37)	12·26(40)	13·60(32)	19 38(51)	0·31(4)	0·01(1)	100·63	66·4
	Ilm	8	0·20(3)	53·30(40)	0·29(1)	41·40(30)	4·86(7)	0·26(3)	0·0(0)	0·03(1)	100·34	97·7

(continued on next page)

Table 2: continued

Run no.[a]	Ph[b]	*n*[c]	SiO_2	TiO_2	Al_2O_3	FeO*	MgO	CaO	Na_2O	K_2O	Total	*X*Ph[d]
Fe-63†	Liq	16	48·91(25)	5·05(22)	11·67(14)	16·90(24)	4·06(7)	9·63(7)	2·87(5)	0·56(3)	99·65	31·2
	Ol	15	35·77(17)	0·10(4)	0·09(5)	35·59(33)	28 75(38)	0·52(5)	0·03(3)	0·01(1)	100·86	59·0
	Plag	16	53 99(38)	0·22(3)	28·40(15)	0·85(15)	0·19(2)	11·38(22)	4·92(13)	0·21(2)	100·16	55·4
	Cpx	8	49·71(84)	2·14(40)	2·74(59)	11·78(41)	13 68(47)	19·60(69)	0·28(3)	0·01(1)	99·94	67·4
Fe-19	Liq	16	47·87(30)	5·60(27)	10·70(12)	18·88(38)	3·97(4)	9·51(13)	2·82(6)	0·66(4)	100·01	28·5
	Ol	6	36·70(10)	0·17(9)	0·06(3)	36·83(8)	26·72(52)	0·50(1)	0·02(0)	0·0(0)	101·00	56·4
	Plag	20	54·42(28)	0·18(5)	28·08(37)	0·81(18)	0·18(9)	11·59(22)	4·80(13)	0·20(2)	100·26	56·5
	Cpx	10	50·85(88)	1·95(38)	3·22(81)	11·63(85)	13·16(62)	19·84(66)	0·27(4)	0·0(0)	100·92	66·9
	Ilm	8	0·57(5)	53·43(32)	0·47(7)	40·21(28)	4·94(18)	0·46(12)	0·06(5)	0·02(2)	100·14	98·8
Fe-66†	Liq	13	50·73(30)	4·54(16)	10·80(12)	17·92(30)	3 12(4)	8·32(12)	2·97(6)	0·79(3)	99·19	24·8
	Ol	8	35·00(18)	0·17(5)	0·03(1)	42·70(38)	22·21(30)	0·52(3)	0·0(0)	0·0(0)	100·62	48·1
	Plag	20	55·42(32)	0·18(8)	27·18(42)	0·92(32)	0·20(6)	10·70(24)	5·00(12)	0·24(3)	99·84	53·4
	Cpx	15	50·82(72)	1·58(33)	1·64(52)	14·25(28)	13·06(24)	18·59(40)	0·23(3)	0·02(1)	100·20	61·9
	Ilm	8	0·23(2)	52·72(25)	0·23(3)	41·83(23)	3·81(4)	0·46(5)	0·02(2)	0·01(1)	99·31	98·3
Fe-65†	Liq	18	51·34(67)	3·96(18)	10·56(18)	17·97(35)	2·73(5)	8 05(19)	3·02(8)	0·89(5)	98·53	22·3
	Ol	10	33·70(21)	0·19(6)	0·02(1)	46·21(55)	19·30(45)	0·59(5)	0·04(1)	0·02(1)	100·06	42·7
	Plag	18	55·20(45)	0·21(5)	27·15(25)	0·95(16)	0·12(3)	10·40(16)	5·25(14)	0·28(3)	99·56	51·4
	Cpx	12	50·61(22)	1·30(14)	1·39(28)	15·20(39)	12·20(37)	18 11(40)	0·19(5)	0·03(2)	99·03	58·9
	Ilm	8	0·30(1)	51·0(5)	0 26(6)	42·60(22)	3·41(5)	0·44(1)	0·05(2)	0·03(0)	98·09	96·5

Fe-59†	Liq	16	53·92(32)	3·40(15)	10·77(23)	17·57(30)	2·12(5)	7·36(10)	3·22(9)	1·25(5)	99·62	18·5
	Ol	8	33·50(15)	0·30(15)	0·05(1)	50·20(50)	16·70(17)	0·62(4)	0·0(0)	0·01(1)	101·38	37·2
	Plag	20	56·58(35)	0·22(6)	26·13(18)	0·97(13)	0·13(3)	9·86(15)	5·59(8)	0·39(2)	99·87	48·2
	Cpx	19	50·20(50)	1·40(30)	1·60(50)	17·00(50)	11·30(30)	18·40(40)	0·20(2)	0·02(2)	100·12	54·2
	Ilm	12	0·21(8)	51·11(30)	0·38(5)	44·34(43)	2·36(8)	0·53(9)	0·06(3)	0·02(1)	99·01	96·5
Fe-61†	Liq	18	55·83(65)	2·99(17)	10·76(17)	17·04(45)	1·76(5)	6·87(18)	3·10(6)	1·32(8)	99·67	16·2
	Ol	10	33·40(30)	0·40(25)	0·03(2)	52·90(40)	14·20(18)	0·66(3)	0·0(0)	0·02(1)	101·61	32·4
	Plag	20	57·08(34)	0·23(15)	26·34(18)	1·06(15)	0·09(1)	9·62(27)	5·72(12)	0·37(2)	100·51	47·1
	Cpx	11	50 30(40)	1·10(12)	1·30(40)	19·70(30)	10·60(20)	17·00(50)	0·14(2)	0·01(1)	100·15	49·0
	Ilm	8	0·24(2)	51·30(40)	0·19(1)	44·60(30)	2·24(5)	0·37(5)	0·0(0)	0·04(1)	98·98	97·1
Fe-76†	Liq	19	57·51(42)	2·62(8)	11·13(9)	16·31(39)	1 34(4)	5·99(11)	3·25(13)	1·64(4)	99·79	13·4
	Ol	11	32·04(12)	0·14(6)	0·01(1)	55·64(34)	11·86(37)	0·64(5)	0·01(1)	0·01(1)	100·35	27·5
	Plag	18	57·28(60)	0·19(5)	26·24(34)	0·94(7)	0·07(2)	8·85(33)	6·22(20)	0·39(3)	100·18	43·0
	Cpx	14	49·53(43)	1·34(27)	1·20(28)	20·69(36)	9·22(22)	17·70(47)	0·21(3)	0·01(1)	99·90	44·3
	Ilm	11	0·03(3)	51·60(27)	0·14(3)	45·51(38)	1·82(5)	0·19(3)	0·01(1)	0·02(1)	99·32	97·2

[a] The experimental runs are listed as in Table 1. The starting compositions used are SC1 unless marked by * or † which represent SC4 and SC4a respectively (see also Table 1).
[b] Phases present; abbreviations used: Liq, liquid; otherwise as Table 1. Plag refers to the multiple analyses of rim compositions, and Plag‡ to the average composition estimated from multiple analyses of both cores and rims.
[c] Number of analyses.
[d] Numbers represent: *mg*-number × 100 for Liq, with *mg*-number = MgO/(MgO+FeO) and FeO and Fe_2O_3 content calculated by the method of Kilinc *et al.* (1983); *mg*-number × 100 for Cpx and for Ol; An content for Pl; X_{Mt} × 100 for Mt, and X_{Ilm} × 100 for Ilm, both calculated using Stormer (1983).
[e] Numbers in parentheses indicate one standard deviation of replicate analyses in terms of least units cited.

Table 3: Modal proportions and estimates of sodium loss

Run no.	Modal proportions (see text for details)	Na loss (rel%)	Σ(residuals squared)
'FMQ + 1'			
Fe-40	Gl(79·6), Ol(4·5), Pl(15·9)	3·7	0·070
Fe-79	Gl(62·7), Ol(7·3), Pl(25·3), Cpx(4·8)	4·0	0·021
Fe-41	Gl(55·3), Ol(6·5), Pl(27·1), Cpx(8·8), Mt(2·3)	3·0	0·105
Fe-95*	Gl(35·3), Pl(24·5), Cpx(28·6), Mt(9·4), Ilm(2·3)	12·9	0·361
'FMQ'			
Fe-45	Gl(90·8), Ol(1·3), Pl(8·0)	3·4	0·114
Fe-36	Gl(74·7), Ol(6·7), Pl(18·6)	1·4	0·040
Fe-37	Gl(68·3), Ol(8·3), Pl(23·0), Cpx(tr)	4·2	0·059
Fe-35	Gl(64·2), Ol(8·1), Pl(24·6), Cpx(3·1)	2·6	0·156
Fe-39	Gl(57·5), Ol(8·6), Pl(27·2), Cpx(6·7)	1·6	0·140
Fe-44R	Gl(57·1), Ol(8·5), Pl(27·5), Cpx(7·0)	1·8	0 095
Fe-42	Gl(49·1), Ol(9·9), Pl(31·5), Cpx(9·5)	1·8	0·091
Fe-43	Gl(31·7), Ol(9·1), Pl(39·8), Cpx(16 5), Mt(1·2), Ilm(1·7)	1·5	0·050
Fe-21	Gl(39·2), Ol(7·8), Pl(34·7), Cpx(16 4), Mt(tr), Ilm(1·6)	1·6	0·082
Fe-47*	Gl(61·8), Pl(16·6), Cpx(18·7), Mt(1·2), Ilm(1·7)	1·0	0·069
Fe-51†	Gl(41·2), Pl(24·1), Cpx(25·2), Mt(8·0), Ilm(1·6)	7·6	0·111
Fe-49*	Gl(32·7), Pl(26·6), Cpx(31·5), Mt(4·8), Ilm(4 4)	11·3	0·337
Fe-52†	Gl(23·6), Pl(30·4), Cpx(33·4), Mt(11·6), Ilm(1·0)	11·1	0 330
'FMQ – 1'			
Fe-24	Gl(85·2), Ol(3·4), Pl(11·4)	1·1	0·045
Fe-23	Gl(67 6), Ol(8·5), Pl(21·7), Cpx(2·2)	4·9	0·117
Fe-25	Gl(52·0), Ol(10·5), Pl(29·4), Cpx(8·2)	5·5	0·047
Fe-67†	Gl(70·7), Ol(3·7), Pl(14·5), Cpx(9·5), Ilm(1·7)	3·6	0·152
Fe-68†	Gl(58·4), Ol(4·3), Pl(19·5), Cpx(14·8), Ilm(3·1)	3·0	0·046
Fe-71*	Gl(38·9), Ol(2·8), Pl(26·1), Cpx(27·1), Ilm(4·9)	1·1	0·549
Fe-77*	Gl(39·4), Ol(2·6), Pl(25·2), Cpx(27·9), Ilm(4·9)	2·2	0·089
Fe-126*	Gl(39·3), Ol(2·5), Pl(27·9), Cpx(25·6), Ilm(4·7)	5·5	0·320
Fe-136*	Gl(40·8), Ol(tr), Pl(25·8), Cpx(27·8), Mt(0·7), Ilm(4·7)	1·4	0 594
Fe-70*	Gl(32·3), Ol(tr), Pl(29·0), Cpx(32·6), Mt(tr), Ilm(5·8)	0·9	0·624

(continued on next page)

Table 3: continued

Run no.	Modal proportions (see text for details)	Na loss (rel%)	Σ(residuals squared)
'FMQ – 2'			
Fe-16	Gl(83·2), Ol(3·9), Pl(12·9)	2·5	0·303
Fe-15	Gl(63·6), Ol(10·5), Pl(25·9)	2·5	0·206
Fe-56	Gl(46·8), Ol(10·2), Pl(31·6), Cpx(11·4)	7·2	0·845
Fe-62	Gl(33·4), Ol(11·3), Pl(37·9), Cpx(15·9), Ilm(1·6)	4·0	0·048
Fe-63†	Gl(90·0), Ol(1·8), Pl(4·1), Cpx(4·0)	7·3	0·248
Fe-19	Gl(33·2), Ol(11·0), Pl(38·2), Cpx(16·4), Ilm(1·3)	0·0	0·027
Fe-66†	Gl(61·2), Ol(3·8), Pl(18·2), Cpx(13·9), Ilm(2·9)	6·8	0·253
Fe-65†	Gl(51·1), Ol(5·0), Pl(22·3), Cpx(17·5), Ilm(4·1)	6·5	0·117
Fe-59†	Gl(36·0), Ol(7·0), Pl(28·5), Cpx(23·2), Ilm(5·4)	5·1	0·072
Fe-61†	Gl(26·9), Ol(6·6), Pl(32·5), Cpx(27·9), Ilm(6·3)	7·7	0·132
Fe-76†	Gl(20·9), Ol(6·7), Pl(33·6), Cpx(32·6), Ilm(6·2)	3·5	0·386

Phases present: Gl, glass; Ol, olivine; Pl, plagioclase; Cpx, clinopyroxene; Mt, magnetite–ulvöspinel; Ilm, ilmenite–haematite.
Numbers in parentheses represent estimated weight proportion of the relevant phase calculated using the weighted least-squares minimization of Albarède & Provost (1977), for mass balance, using the data and errors presented in Table 2. tr, trace (i.e. >0·5 wt % of the mode).
*,†See Table 2.

temperature by ilmenite, whereas below FMQ ilmenite crystallizes before magnetite. At FMQ+1 magnetite crystallization begins at ~1125°C, but its liquidus temperature falls by ~30°C per log unit decrease in f_{O_2}. Below the FMQ buffer ilmenite has an approximately constant liquidus temperature of ~1100°C, whereas at higher f_{O_2}, where Ilm follows Mt, the Ilm liquidus has a negative slope, falling to ~1080°C at FMQ+1.

Melt compositions

The melt compositions encountered in this study range from basaltic to dacitic, and their compositional variations with temperature are summarized in Figs 3–5. Although data from all the experiments are shown together, attention should be drawn to the effect of using the fractionated composition SC4 on the compositional evolution of the melt phase. All experiments represent a close approach to equilibrium crystallization of the relevant composition (SC1 or SC4). However, the liquid products of the perfect equilibrium crystallization of SC4 are not those of the continued equilibrium crystallization of SC1 because of the 'removal' or 'fractionation' of the solid phases. Equilibrium and fractional crystallization paths may be expected to diverge with falling temperature to produce different liquid and solid composition, and this must be borne in mind when considering Figs 3–5.

The concentrations of K_2O, Na_2O, MgO and CaO in the experimental liquids, shown in Figs 3a–d, are insensitive to f_{O_2}. Potassium and sodium are both enriched in the melt phase as crystallization proceeds, with K_2O increasing from 0·3 wt % at the liquidus to a maximum of 1·85 wt % K_2O at 1060°C (Fig. 3a), and Na_2O varying from 2·7 to 3·6 wt % Na_2O over the same temperature range (Fig. 3b). Experiments at FMQ−2 show lower values and more scatter in Na_2O, reflecting the higher volatility of sodium at reducing conditions. MgO and CaO both fall in concentration with decreasing temperature. MgO content falls approximately linearly with temperature, from 6 wt % at 1160°C, to 1·5 wt % at 1050°C (Fig. 3c), whereas melt CaO content rises at temperatures just below the liquidus, but falls once clinopyroxene begins crystallizing (Fig. 3d). The CaO content of melts cosaturated in olivine, clinopyroxene and plagioclase decreases linearly with temperature, a feature observed in both natural and

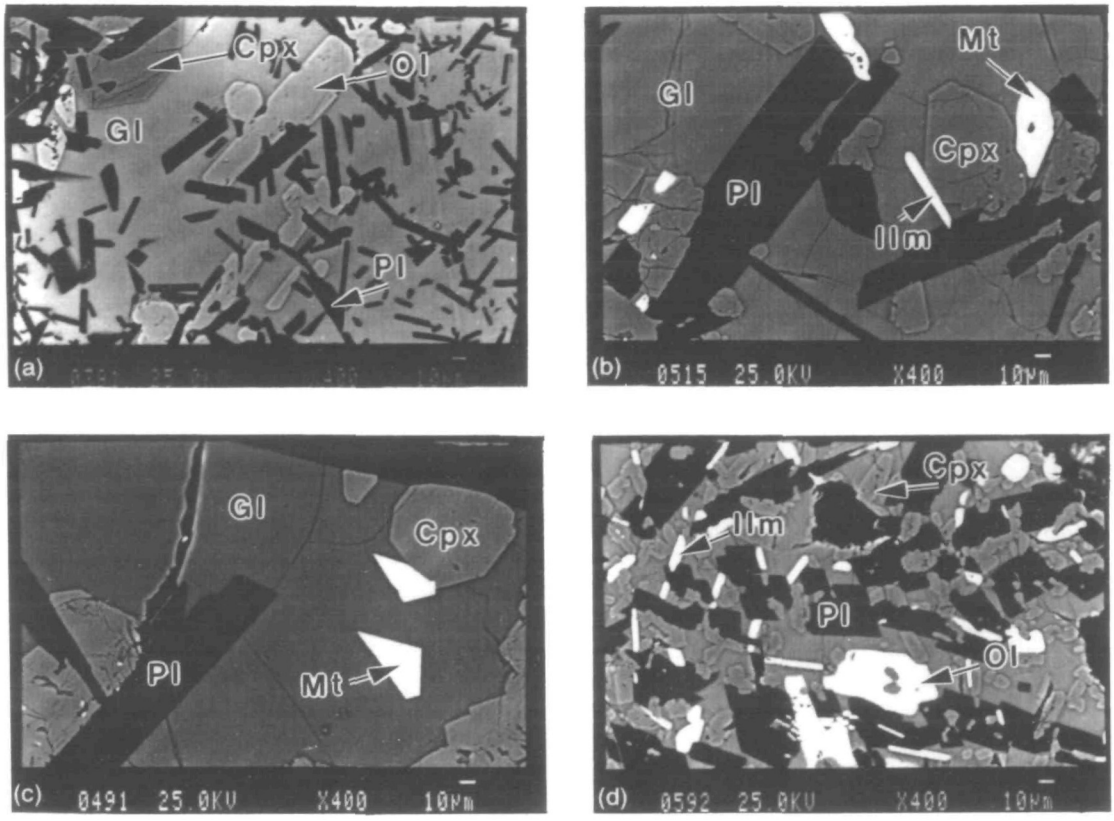

Fig. 1. Back-scattered electron images of typical quenched run products with examples of the crystalline phases observed. All photos are the same scale (×400: see 10-μm scale bar), thus showing variation in phase size and texture. (a) Sample Fe-39: FMQ, 1115°C. (b) Sample Fe-51: FMQ, 1078°C. (c) Sample Fe-49: FMQ, 1068°C. (d) Sample Fe-59: FMQ-2, 1071°C. Gl, glass; Ol, olivine; Pl, plagioclase; Cpx, calcium-rich clinopyroxene; Mt, magnetite–ulvöspinel solid solution; Ilm, ilmenite–haematite solid solution.

synthetic systems (Helz, 1987; Shi and Libourel, 1991). However, with falling temperature the calcium contents of melts lacking olivine (i.e. using SC4, at and above FMQ) show consistently lower values than those observed in olivine-saturated melts.

The titanium, iron, aluminium and silica contents of the liquid depend on both temperature and f_{O_2}, and Figs 4a–c show variations as contoured concentration maps on a T–f_{O_2} plane. The liquidus boundaries for the various crystalline phases are also shown, to highlight the relationship between phase appearances and variations of melt composition. The melt TiO_2 contents (Fig. 4a) increase during the early stages of crystallization, before Fe–Ti oxide crystallization. Below the FMQ buffer the TiO_2 content of the melt reaches a maximum of 5–5·5 wt% at ~1100°C, coinciding with the appearance of ilmenite on the liquidus, and then falls rapidly with further temperature decrease. Above FMQ, maximum melt TiO_2 concentrations are <5 wt%; they are little affected by Mt crystallization and do not begin to decrease until Ilm begins to crystallize. The melt iron contents (FeO* = total iron as FeO; Fig. 4b) show general behaviour similar to that observed for TiO_2, also initially increasing with decreasing temperature, then falling rapidly at lower temperatures. With increasing f_{O_2} the temperature of the FeO* maximum increases, and the magnitude of the maximum decreases (e.g. from ~15 wt% FeO* at FMQ+1, to ~18·5 wt% FeO* at FMQ−2). Above FMQ the maximum iron content coincides with the appearance on the liquidus of magnetite. Below FMQ, where ilmenite is the first crystallizing Fe–Ti oxide phase, there is a broad maximum in iron content of ~18·5 wt% FeO* occurring on the low-temperature side of the ilmenite-in boundary. The crystallization of ilmenite does not abruptly terminate iron enrichment, as is the case with magnetite at higher f_{O_2}, but its presence does limit, and finally terminate the continued iron enrichment of the liquid. The silica content of the liquid (Fig. 4c) varies from its initial value of just over 48 wt% SiO_2 to a maximum value of 65 wt% SiO_2. The silica content of the liquid remains approximately constant throughout the early stages of crystallization, but

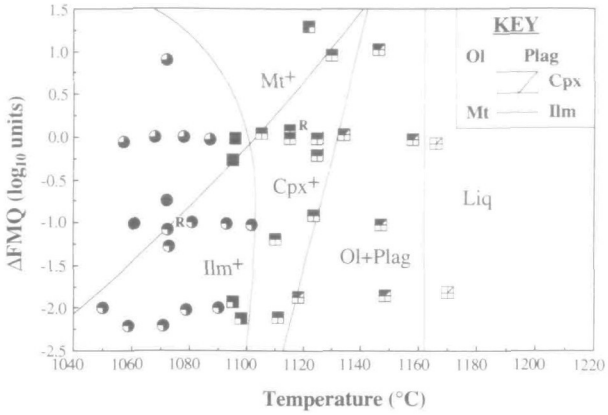

Fig. 2. Experimentally determined phase equilibria for compositions SC1 and SC4 as a function of temperature and oxygen fugacity (log f_{O_2} relative to FMQ buffer). Squares indicate experiments using SC1 starting composition, circles indicate SC4 starting composition (see Tables 1 and 2 for details). All experiments contain liquid (Liq) in addition to the crystalline phases indicated by the symbol filling (see key: Ol, olivine; Plag, plagioclase; Cpx, calcium-rich clinopyroxene; Mt, magnetite–ulvöspinel solid solution; Ilm, ilmenite–haematite solid solution). The continuous lines mark inferred phase boundaries. Above the FMQ buffer the appearance temperature for ilmenite has been drawn using data from an experiment at FMQ+1·8, at 1072°C which does not contain ilmenite on the liquidus at these conditions, described by Toplis *et al.* (1994). R marks reversal experiments described in Table 1.

increases rapidly at high f_{O_2} when magnetite is the first crystallizing Fe–Ti oxide. At low f_{O_2} the crystallization of ilmenite causes a similar enrichment of silica in the liquid. The alumina content of the melts shows a broad minimum, which deepens from 11·5 wt% Al_2O_3 at FMQ+1 and ~1110°C, to 10·5 wt% Al_2O_3 at FMQ−2 and ~1070°C. Minimum aluminium concentrations are not directly correlated with the appearance of any one particular crystalline phase, but are roughly correlated with the peak iron concentrations below the FMQ buffer.

The concentrations of iron and silica in the melt are sensitive to the crystallization of the Fe–Ti oxides (Figs 4b and c), but the different oxide minerals have different effects on melt composition trends as shown in Fig. 5, where the tie-lines join melts from different f_{O_2} but the same temperature. Before saturation of an Fe–Ti oxide, iron enrichment in the experimental melts proceeds at approximately constant SiO_2 content at all the studied f_{O_2}. However, with further decrease of temperature, the compositions of ilmenite- and magnetite-saturated melts diverge. For evolution parallel to FMQ, magnetite saturation causes an immediate depletion of iron (from ~17 wt% FeO*), and enrichment of silica in the melt. Ilmenite saturation also results in an

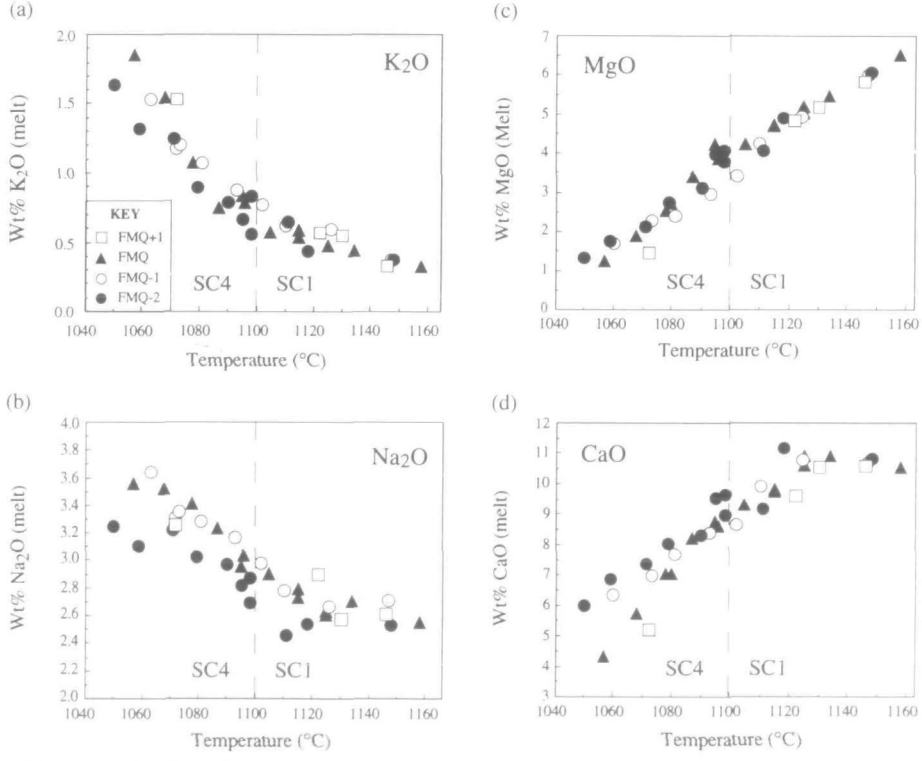

Fig. 3. Melt compositions as a function of experimental temperature. (a) wt% K_2O. (b) wt% Na_2O. (c) wt% MgO. (d) wt% CaO. Experiments at different oxygen fugacities are distinguished as shown in the key. The errors on the measurements are typically the size of the symbols.

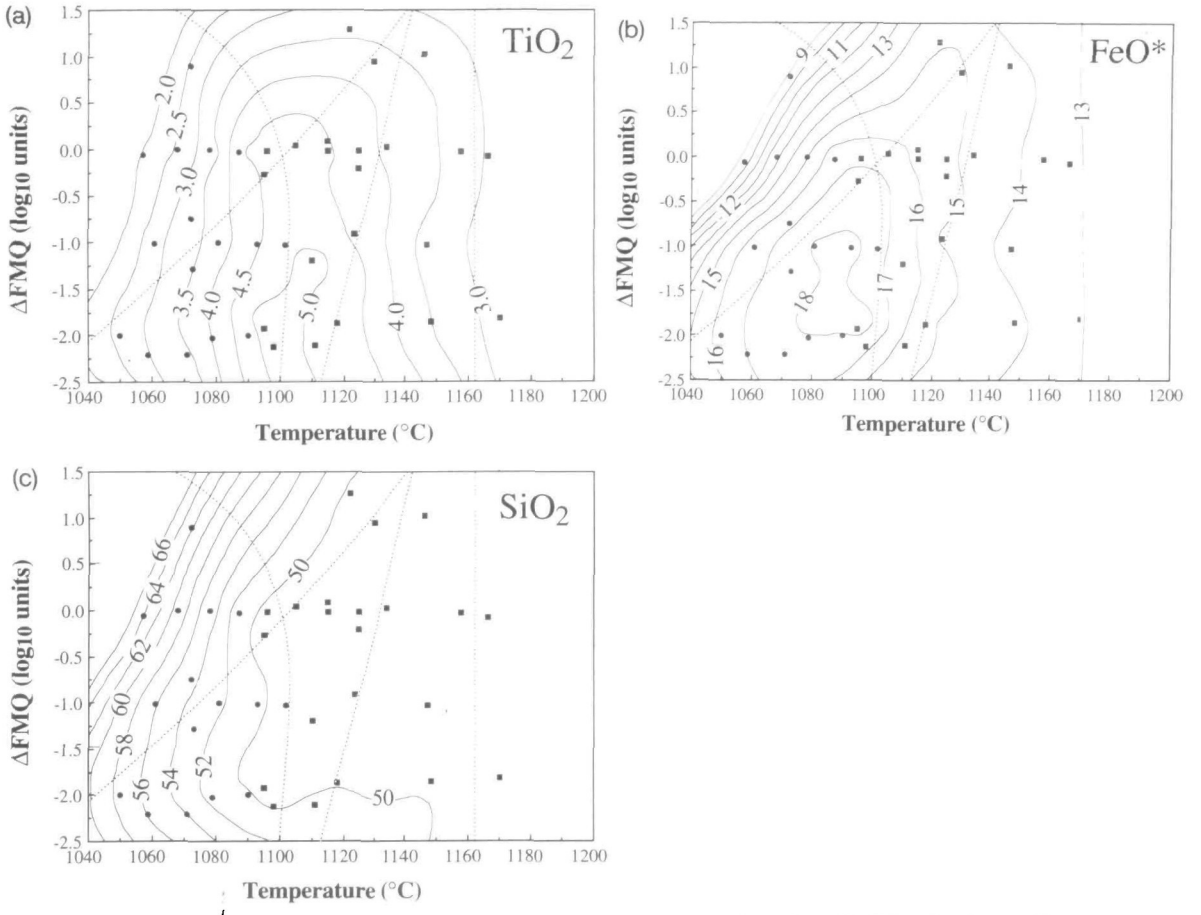

Fig. 4. Melt compositions as function of T and f_{O_2}. (a) wt % TiO_2. (b) wt % FeO*. (c) wt % SiO_2. Continuous lines are contours of wt % oxide component, based on data presented in Table 2. Dashed lines are the inferred phase boundaries from Fig. 2 and symbols indicate data points used for contouring. Data from all experiments have been used to produce this contour plot, although it should be borne in mind that the liquid line of descent of the fractionated composition SC4 is not the same as that which would be produced by the continued equilibrium crystallization of SC1 at these temperatures.

immediate increase of SiO_2 content, but FeO contents continue to rise to a peak of ~18·5 wt %. Thus, for the same temperature drop, Mt-saturated melts show a larger decrease in FeO* than do Ilm-saturated melts (changes in melt silica content are similar). Magnetite saturation therefore leads to more 'evolved' (i.e. SiO_2-rich, FeO*-poor) melt compositions than those produced by ilmenite saturation at the same temperature.

Mineral compositions

Plagioclase compositions are shown as a function of temperature in Fig. 6. The anorthite content falls from An_{75} near the liquidus, to An_{45} at 1050°C, and appears to be independent of f_{O_2}. The variation in An content is small when only plagioclase and olivine are on the liquidus, but once the melt is saturated in Cpx, the plagioclase An content decreases by ~5% An per 10°C drop in temperature. In detail, plagioclases from experiments using SC1 are observed to be more anorthitic than those produced at the same temperature from experiments using SC4, thus causing the 'step' in the trend shown in Fig. 6 at ~1100°C. This may be explained by the use of SC4, which introduces a fractional 'step' in the crystallization path of SC1. Iron occurs as a minor component (typically <1 wt % FeO*). Above 1100°C the plagioclases from experiments at higher f_{O_2} are generally the most iron rich, although plagioclases from lower-temperature experiments do not exhibit any systematic relation between FeO* content and f_{O_2}. The orthoclase content of the plagioclases is typically low, but increases with falling temperature as the K_2O content of the liquid increases, reaching Or_2 (0·4 wt % K_2O) at 1050°C. MgO and TiO_2 are present in low concentrations; typically 0·1–0·4 wt % MgO, and 0·2 wt % TiO_2.

The compositions of experimental olivines vary

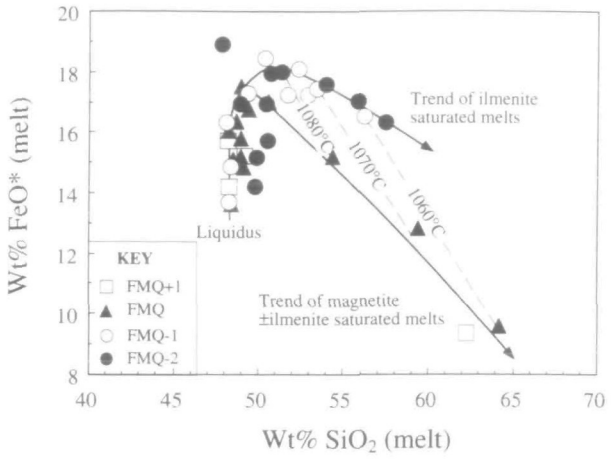

Fig. 5. The covariation of iron (FeO* = total iron as FeO) and silica in experimental melts. Trends for magnetite- and ilmenite-saturated melts are indicated by continuous curves, and dashed lines indicate isotherms connecting ilmenite- and magnetite(±ilmenite)-saturated melts (see discussion in text).

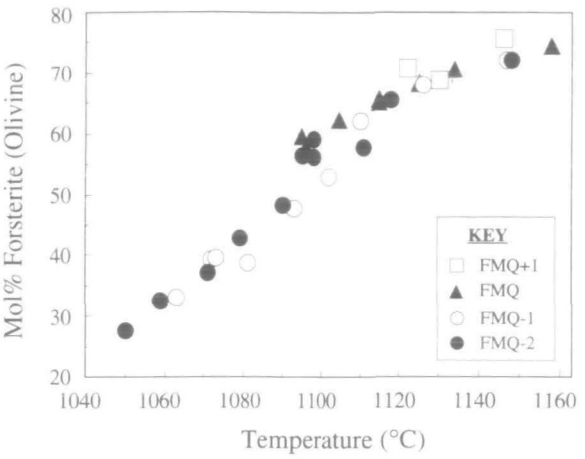

Fig. 7. Mole % forsterite in experimental olivines as a function of temperature, with different oxygen fugacities distinguished as shown in the key. The height of the symbols corresponds to the average error in measured forsterite contents (approximately ±1 mol % Fo).

from Fo_{75} at the liquidus to Fo_{27} at 1050°C (Fig. 7). The composition of olivines from experiments at and below the FMQ buffer appears to be independent of f_{O_2}, although olivines from experiments at FMQ+1 are generally more forsterite rich (probably owing to the greater ferric-iron content of these more oxidized liquids). The forsterite content (at fixed T) of olivines from experiments using SC1 is greater than that of olivines from experiments using SC4, thus causing a 'step' in the trend shown in Fig. 7, similar to that observed for the An content of plagioclase (Fig. 6). Calcium is the only minor constituent of the olivine, and is typically 0·5 wt % CaO; crystal–melt partitioning of calcium is discussed further below.

The compositions of the pyroxenes are shown in Fig. 8 in an expanded portion of the pyroxene quadrilateral. The first crystallizing clinopyroxene along the FMQ buffer has an *mg*-number of 74 at 1125°C, falling to 54 at 1057°C, and Ca content varies between Wo_{41} and Wo_{34} and shows a minimum near 1100°C at an *mg*-number of 67. At FMQ−2 the first crystallizing pyroxene has an *mg*-number of 69, falling to 44 at 1050°C. The calcium content of pyroxenes at both FMQ−1 and FMQ−2 initially decreases with decreasing temperature, but at both oxygen fugacities a broad minimum occurs

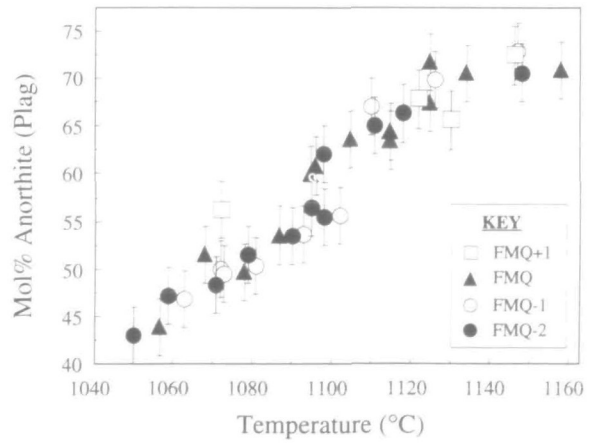

Fig. 6. Mole % anorthite in experimental plagioclases as a function of temperature, with different oxygen fugacities distinguished as shown in the key. The error bars correspond to ±3 mol % anorthite and are typical of the average experimental uncertainty.

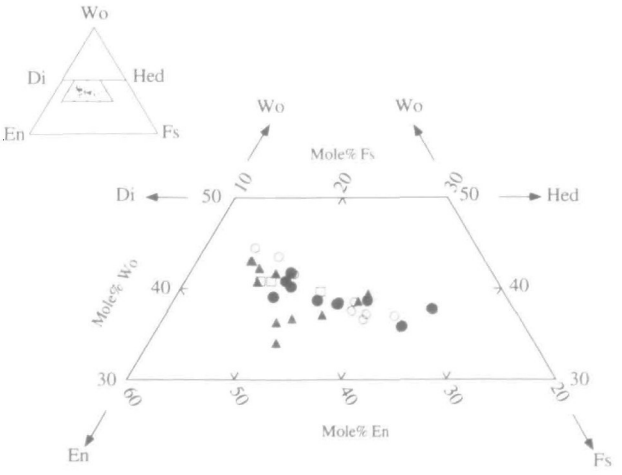

Fig. 8. The composition of experimental pyroxenes plotted in an expanded portion of the pyroxene quadrilateral (see inset). The presence of minor concentrations of aluminous end-member pyroxenes (e.g. CaTs molecule and jadeite) has not been taken into account, and mol % Wo, En and Fs are calculated from the normalized mol % of the components Ca, Mg and Fe, respectively. Different symbols correspond to different oxygen fugacities, as indicated for Fig. 7.

at Wo_{37}. The position of this minimum moves to lower *mg*-number with decreasing f_{O_2}, from *mg*-number ~56 at FMQ−1, to *mg*-number ~49 at FMQ−2. Minor components in clinopyroxene include 0·25 ± 0·05 wt% Na_2O, ~4–1 wt% Al_2O_3 and ~2·5–1 wt% TiO_2, with the last two showing a general decrease with decreasing temperature, but no obvious dependence on f_{O_2}. The stoichiometry of the Cpx produced in experiments above the FMQ buffer suggests that they may also contain significant ferric iron. Assuming an ideal pyroxene stoichiometry of $M_2T_2O_6$ [where M are octahedral cations, e.g. Mg, Ca, Al(VI); T are tetrahedral cations, e.g. Si, Al(IV); O is oxygen] and assigning all iron to be ferrous yields an excess of cations for these pyroxenes. The ferric iron required to return them to stoichiometric values is: 2 wt% Fe_2O_3 (18% of FeO* as Fe_2O_3) for Fe-79; 3 wt% Fe_2O_3 (29% of FeO* as Fe_2O_3) for Fe-41; and 2 wt% Fe_2O_3 (14% of FeO* as Fe_2O_3) for Fe-95. For pyroxenes grown at $f_{O_2} \leqslant$ FMQ cation sums are 4·000 ± 0·008 per 6 oxygens, suggesting that ferric iron is not an important constituent.

The compositions of Fe–Ti oxides, recalculated following Stormer (1983), are shown as a function of f_{O_2} in Figs 9a and b. At conditions parallel to the FMQ buffer the recalculated X_{Mt} and X_{Ilm} remain approximately constant, and do not show any systematic variation with temperature. For example, along the FMQ buffer Mt and Ilm vary in the range Mt_{22-25} and Ilm_{91-92}, and at FMQ−2 ilmenites vary from Ilm_{97} to Ilm_{98}. The ferric iron content of both phases increases with f_{O_2}, but at a fixed f_{O_2} the ferric iron content of magnetite is always greater than that of ilmenite, the difference becoming greater with increasing f_{O_2}. The MgO contents of ilmenites and magnetites vary from 5 to 2 wt%, and fall with decreasing temperature, following the decreasing *mg*-number of the liquid, but at a fixed temperature ilmenite is always more MgO rich than the coexisting magnetite. The aluminium content of magnetite also falls with decreasing temperature, from ~4 wt% Al_2O_3 at 1120°C to slightly less than 2 wt% Al_2O_3 at 1060°C.

Mineral modes: the growth and resorption of crystalline phases

The weight fractions of melt and coexisting crystalline phases have been estimated for each experiment using the weighted least-squares mass balance minimization of Albarède & Provost (1977). These values are presented in Table 3 and shown graphically in Figs 10–14. The variation of mineral abundance as a function of temperature may be used to distinguish

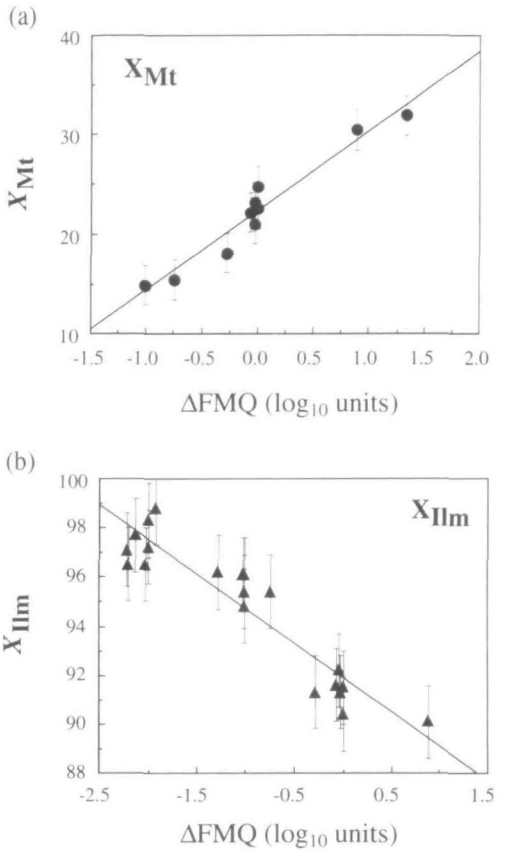

Fig. 9. (a) X_{Mt} in the solid solution magnetite–ulvöspinel. (b) X_{Ilm} in the solid solution ilmenite–haematite. Both calculated using Stormer (1983).

crystallizing solid phases from resorbing solid phases, but it should be borne in mind that the results of these calculations must be supported by evidence from the experimental charges, e.g. if phase resorption is implied there should be textural evidence to support this.

The estimated liquid proportions of experiments using SC1 and SC4, shown as a function of temperature in Fig. 10a, indicate ~1 wt% crystallization per 1°C drop in temperature for both starting compositions. This result is apparently independent of f_{O_2} despite the fact that at a given temperature, different stable phase assemblages, and very different liquid compositions are present. The 1σ error on the calculated liquid abundances is typically 2 wt% (absolute). The calculated liquid proportion from experiments using SC4 may be scaled by an appropriate value to estimate the percentage of liquid remaining from crystallization of SC1 over the entire studied temperature interval. When SC4 is at its liquidus (100% liquid), it has the same composition as the residual liquid of SC1 after ~43% crystallization (57% liquid); the liquid pro-

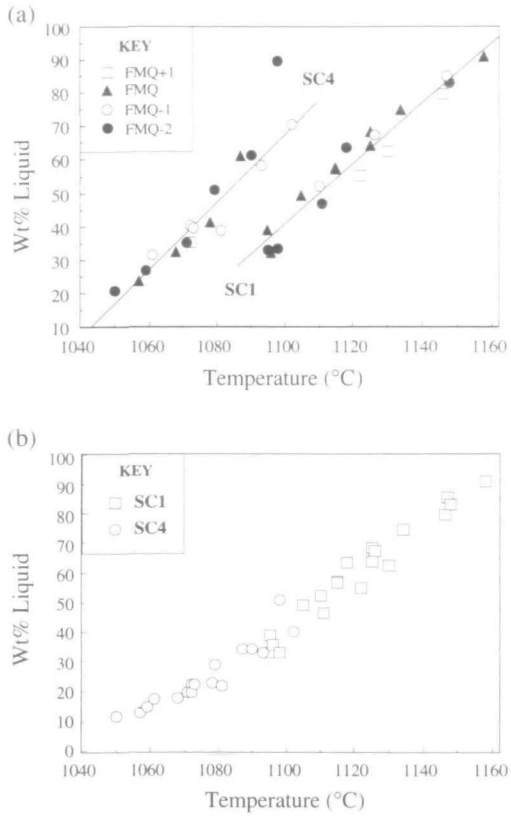

Fig. 10. (a) Calculated liquid proportion as function of temperature for experiments using SC1 and SC4 starting compositions (see Table 3 and text for details of the calculations). Differences in experimental f_{O_2} are indicated by symbol differences (see key). (b) Calculated liquid fraction for all experiments, with results from more evolved SC4 composition (on the liquid line of descent of SC1) scaled by the factor 0·57 to compare the estimated liquid proportion of experiments using the two different starting compositions (SC4 has a liquidus temperature of ~1115°C at which time SC1 contains an estimated 57% liquid). (See text for further discussion.)

portion of experiments using SC4 may thus be scaled by the factor 0·57 to obtain an estimate of the liquid proportion of SC1 which would have been present at that temperature. Figure 10b shows the liquid proportions from experiments using SC1, and scaled values from experiments using SC4. The combined data are observed to lie on a continuous trend with falling temperature, and Fig. 10b suggests that although crystallization of SC1 takes place at ~1% crystallized per °C over the first 70°C below the liquidus, at lower temperature the percent crystallized per degree centigrade decreases as the solidus is approached. This behaviour is almost identical to that calculated by Ghiorso & Carmichael (1985) using a Gibbs free energy minimization model for the crystallization of an olivine tholeiite over the first 90% of its crystallization.

The calculated abundances of plagioclase and clinopyroxene increase with decreasing temperature, as shown in Fig. 11. The plagioclase mode is independent of f_{O_2}, whereas, at a given temperature, the proportion of Cpx is lowest in experiments carried out at FMQ − 2, and highest in those carried out at FMQ + 1. This may be explained by the variation of the appearance temperature of Cpx as a function of f_{O_2} as shown in Fig. 2. The rate of increase of the modal proportion of Cpx as a function of temperature, however, has a similar magnitude at all the studied f_{O_2}.

In contrast to plagioclase and clinopyroxene, the calculated abundance of olivine does not continuously increase with falling temperature. Figure 12 shows that from 1160°C to ~1110°C the abundance of olivine increases with falling temperature, and is independent of f_{O_2}. However, at ~1110°C along the FMQ buffer the calculated absolute modal abundance of olivine begins to fall, implying resorption. This is supported by the fact that at FMQ, experiments performed using SC4 do not contain olivine. In addition, backscattered electron images of

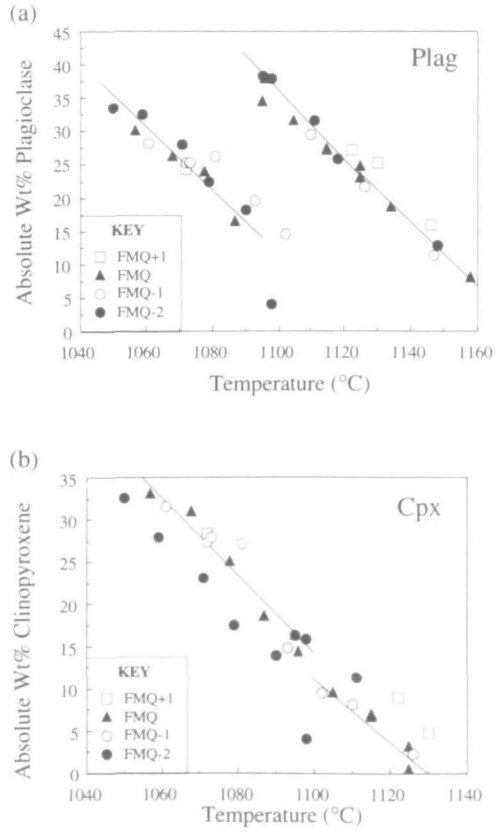

Fig. 11. Absolute modal abundances (wt %) as a function of temperature for (a) plagioclase, and (b) clinopyroxene, estimated using mass balance constraints described in Table 3 and the text. Different lines indicate trends for the two starting compositions used.

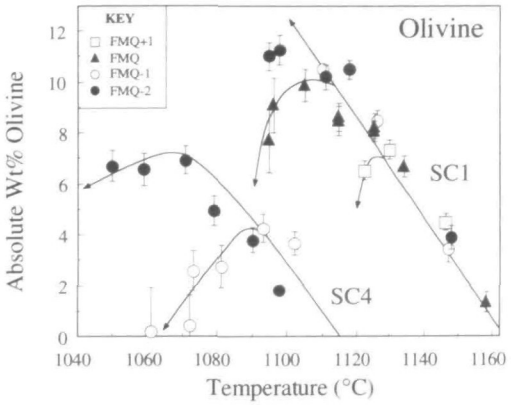

Fig. 12. Absolute modal abundances (wt %) of olivine as a function of temperature, estimated using mass balance constraints. The error bars shown are those calculated by the weighted least-squares mass balance calculations using the minimization procedure of Albarède & Provost (1977). The lines trace the variation of absolute wt % abundance of olivine for each studied f_{O_2}. Decreasing abundance implies resorption. Resorption is inferred for all the studied f_{O_2}, although the onset of resorption moves to lower temperature with decreasing f_{O_2}.

the textures of experimental olivines (Figs 13a–d) show a change from euhedral to rounded crystal shape, further supporting resorption at lower temperature. Based on downturns in modal abundance vs temperature (Fig. 12), the onset of resorption is inferred to occur at ~1100°C at FMQ−1, and at ~1070°C at FMQ−2. Thus there is evidence for the resorption of olivine at all the studied f_{O_2}. The temperature of onset of resorption is a function of f_{O_2} and moves to lower temperature with decreasing f_{O_2}. Furthermore, the mass balance calculations suggest that resorption of olivine is more pronounced at higher f_{O_2}. Olivine resorption does not appear to be associated with the immediate crystallization of another solid phase, although it is noted that magnetite crystallization occurs soon after the onset of olivine resorption at all f_{O_2}.

The calculated modal abundances of ilmenite and magnetite as a function of temperature are shown in Figs 14a and 14b, respectively. Within the errors of the estimates the abundance of ilmenite rises approximately linearly with falling temperature at FMQ−1 and FMQ−2. In contrast, the data from FMQ and FMQ+1 suggest that ilmenite crystallization is inhibited by the presence of magnetite, and that the abundance of ilmenite may even decrease with falling temperature (for crystallization parallel to the FMQ buffer). The modal abundance of magnetite (shown in Fig. 14b) increases with falling temperature, but the strong dependence of

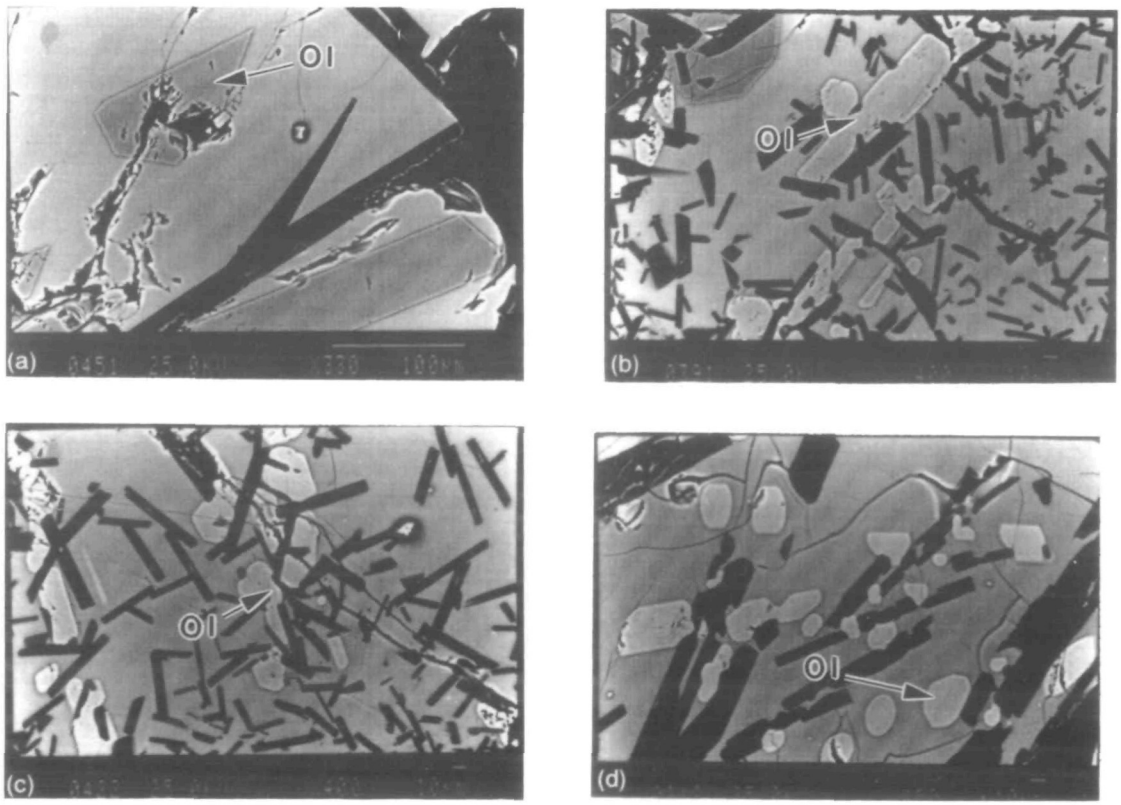

Fig. 13. Backscattered electron images of experiments along the FMQ buffer showing the resorption of olivine with falling temperature. (a) Sample Fe-45: 1158°C. (b) Sample Fe-39: 1115°C. (c) Sample Fe-42: 1105°C. (d) Sample Fe-21: 1095°C.

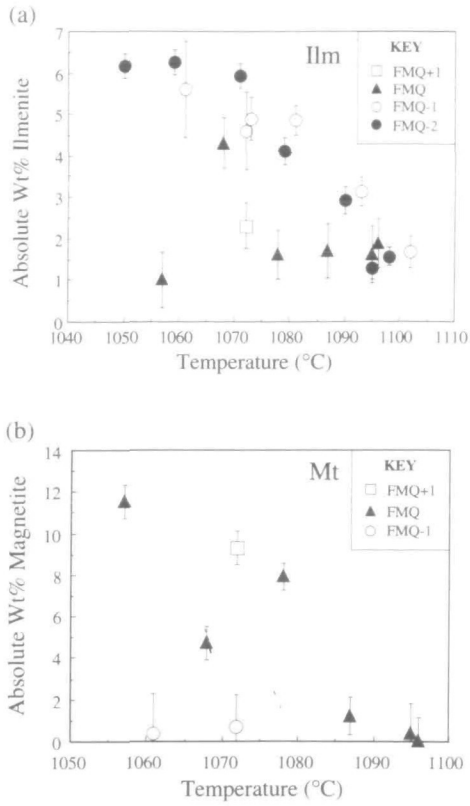

Fig. 14. Absolute modal abundances (wt %) as a function of temperature for (a) ilmenite and (b) magnetite, estimated from mass balance calculations. The error bars represent 1σ errors as estimated from the weighted least-squares minimization of Albarède & Provost (1977).

the magnetite saturation temperature on f_{O_2}, and the large error associated with the estimation of magnetite proportion make quantification of the rate of change of magnetite abundance with temperature difficult.

DISCUSSION

Major element partitioning between silicates and coexisting melts

Element partitioning between the common igneous minerals and silicate liquids has been extensively studied because of the applicability of such data to geothermometry and testing for phenocryst–groundmass equilibrium. Although many data exist in the literature, most of the studied systems are relatively rich in magnesium, and little is known concerning mineral–melt equilibria at low melt *mg*-number.

Mg–Fe partitioning between olivine and melt

Owing to the importance of olivine in many igneous processes the partitioning of divalent cations between olivine and basaltic melts has been widely studied (e.g. Roeder & Emslie, 1970; Leeman & Scheidegger, 1977; Gee & Sack, 1988; Jurewicz & Watson, 1988), and the compositions of olivine–glass pairs are widely used as a test for phenocryst–groundmass equilibrium in both experimental and natural systems. A partition coefficient $K_{dFe\text{-}Mg}^{Ol\text{-}Liq}$, defined as $(X_{Ol}^{FeO}/X_{Ol}^{MgO} \cdot X_{Liq}^{MgO}/X_{Liq}^{FeO})$, where X indicates mole fraction, may be used to describe the distribution of magnesium and iron between silicate liquid and coexisting olivine. Roeder & Emslie (1970) observed that at equilibrium $K_{dFe\text{-}Mg}^{Ol\text{-}Liq}$ has a value of $0{\cdot}30 \pm 0{\cdot}02$ which is largely independent of temperature and melt composition. Although more recent studies have shown that $K_{dFe\text{-}Mg}^{Ol\text{-}Liq}$ varies with melt composition, in particular the level of silica undersaturation (Gee & Sack, 1988), it is still generally agreed that in basaltic systems $K_{dFe\text{-}Mg}^{Ol\text{-}Liq}$ does not show a large dependence on temperature or melt composition. However, several experimental studies in iron-rich systems have reported high values of $K_{dFe\text{-}Mg}^{Ol\text{-}Liq}$ at low *mg*-number. Some workers have interpreted these high values as artefacts caused by disequilibrium or iron loss during experiments (Longhi & Pan, 1988; Shi, 1993), and others have believed them to be real, and attributed them to non-ideality in the melt, as a result of the proximity to regions of low-temperature liquid immiscibility in iron-rich systems (Hoover & Irvine,1977).

Figure 15a shows $K_{dFe\text{-}Mg}^{Ol\text{-}Liq}$ data from this study, plotted as a function of the *mg*-number of the coexisting melt. The ferric-iron content of the melt has been estimated following Kilinc *et al.* (1983), and the ferric iron content of the olivine is assumed to be negligible. The calculated values of $K_{dFe\text{-}Mg}^{Ol\text{-}Liq}$ do not exhibit any consistent variation with f_{O_2}, in agreement with the study of Snyder & Carmichael (1992). For values of *mg*-number(melt) >30 the observed $K_{dFe\text{-}Mg}^{Ol\text{-}Liq}$ is approximately constant at $0{\cdot}32 \pm 0{\cdot}02$, in agreement with previous results (e.g. Roeder & Emslie, 1970). However, olivines coexisting with liquids of *mg*-number <30 show progressively higher values of K_d, reaching 0·4 when the *mg*-number of the liquid is 15. Given that our experimental K_d values agree well with the accepted values for the more magnesian melts, and our evidence for close approach to equilibrium, with minimal iron loss (Table 3), we believe that the observed increase in $K_{dFe\text{-}Mg}^{Ol\text{-}Liq}$ for liquids of *mg*-number <30 is real and not an experimental artefact. The effect of temperature on $K_{dFe\text{-}Mg}^{Ol\text{-}Liq}$ over the studied range is less than the error on an individual measured value of $K_{dFe\text{-}Mg}^{Ol\text{-}Liq}$, and may therefore be neglected. Furthermore, we may assess the suggestion of Hoover & Irvine (1977) that the observed increase is due to non-idealities of Fe–Mg mixing in the melt,

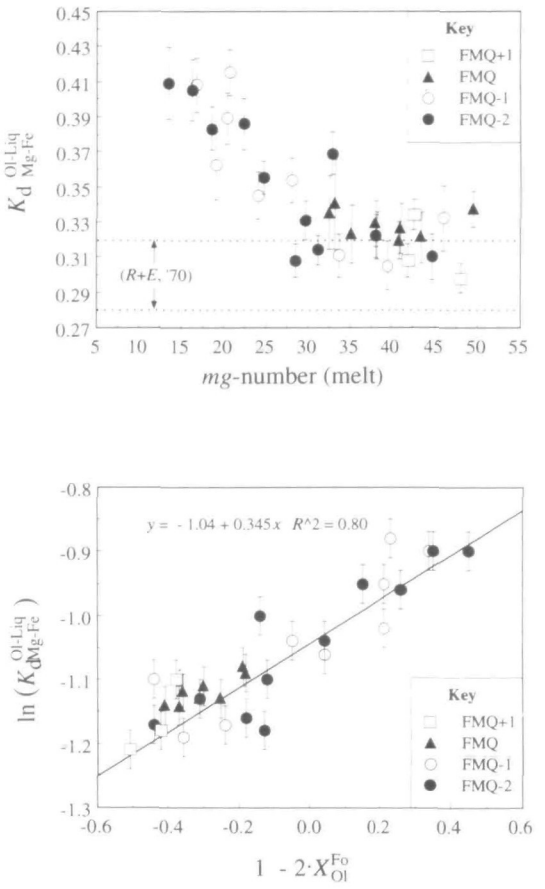

Fig. 15. (a) The variation of $K_{dFe\text{-}Mg}^{Ol\text{-}Liq}$ with *mg*-number of the melt. The dashed lines enclose the range of typical values for basaltic melts (0·3 ± 0·02), taken from Roeder & Emslie (1970). The error bars have been calculated from the standard deviation of MgO and FeO shown in Table 2. Both $K_{dFe\text{-}Mg}^{Ol\text{-}Liq}$ and *mg*-number(melt) have been calculated taking into account the ferric iron content of the liquid, estimated using the calculation scheme of Kilinc *et al.* (1983). (b) The variation of $K_{dFe\text{-}Mg}^{Ol\text{-}Liq}$ as a function of 1–2 X_{Fo} of the experimental olivines. Line shows least-squares fit to data and slope corresponds to W/RT, where W is a symmetric interaction parameter describing the non-ideality of Fe–Mg mixing on the olivine, R is the gas constant, and T is the temperature in K. (See text for more details.)

an alternative possibility being that the observed variation of $K_{dFe\text{-}Mg}^{Ol\text{-}Liq}$ is caused by non-idealities of Fe–Mg mixing in the olivine.

Mixing between iron and magnesium in olivine is known to be non-ideal, and may be described by a single symmetric interaction parameter W of ~4 kJ/mol (Wood & Virgo, 1989; Wiser & Wood, 1991). If we consider the exchange reaction

$$\underset{\text{(olivine)}}{MgSi_{0\cdot5}O_2} + \underset{\text{(melt)}}{FeO} \leftrightarrow \underset{\text{(olivine)}}{FeSi_{0\cdot5}O_2} + \underset{\text{(melt)}}{MgO} \qquad (1)$$

and assume that non-idealities in the melt are negligible, then it may be shown (e.g. Wiser & Wood, 1991) that the measured values of ln $K_{dFe\text{-}Mg}^{Ol\text{-}Liq}$ should be a linear function of $[1-2X_{MgSi_{0\cdot5}O_2}$ (olivine)]. If these assumptions are valid then a plot of ln $K_{dFe\text{-}Mg}^{Ol\text{-}Liq}$ vs $[1-2X_{MgSi_{0\cdot5}O_2}$ (olivine)] should be linear, with a slope of W/RT, where W is the symmetric interaction parameter, R is the gas constant, and T is the absolute temperature. This is illustrated in Fig. 15b, which shows that the value of W calculated from our partitioning data (4·2 ± 0·6 kJ/mol) agrees well with the directly measured value (3·7 ± 0·8 kJ/mol). This implies that the non-ideality of Fe–Mg mixing in olivine can explain the observed variation of $K_{dFe\text{-}Mg}^{Ol\text{-}Liq}$ without the need to infer non-idealities in the melt.

Calcium partitioning between olivine and melt

Calcium is a ubiquitous minor component of olivine, and Ca partitioning between silicate liquids and coexisting olivines has been experimentally determined by Jurewicz & Watson (1988). They found $D_{CaO}^{Ol\text{-}Liq}$ (defined as wt % CaO^{Ol}/wt % CaO^{Liq}) to be a linear function of the olivine Fo content in the range Fo_{90}–Fo_{55}. Figure 16 shows that the agreement between the values of $D_{CaO}^{Ol\text{-}Liq}$ from our experimental olivines and the model of Jurewicz & Watson (1988) is good for the range of olivine compositions over which the model was calibrated, but that more iron-rich compositions show higher values of $D_{CaO}^{Ol\text{-}Liq}$ than predicted. Our experimental data suggest that a linear dependence of $D_{CaO}^{Ol\text{-}Liq}$ on the forsterite content is not appropriate for olivines more iron rich than Fo_{55}, as also demonstrated by Snyder & Carmichael (1992).

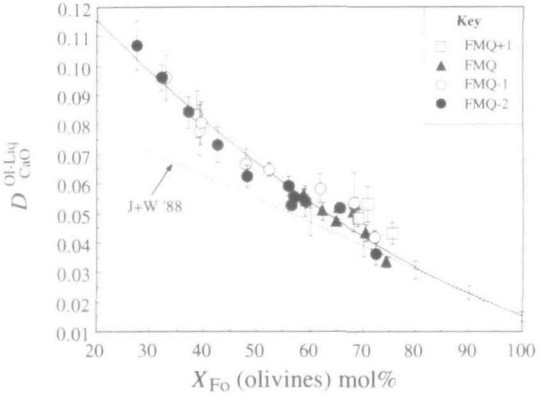

Fig. 16. The variation of $D_{CaO}^{Ol\text{-}Liq}$ as a function of the forsterite content of the olivines. The dashed line (J+W '88) marks the predicted variation of $D_{CaO}^{Ol\text{-}Liq}$ (with quoted errors) as a function of olivine composition from the experimental results of Jurewicz & Watson (1988). The error bars on the experimental data from this study have been estimated from the standard deviation of CaO concentrations shown in Table 2. The continuous line shows a second-order polynomial fit to the experimental data, constrained to pass through the Jurewicz & Watson (1988) data at high forsterite contents.

Mg–Fe partitioning between pyroxene and melt

The partitioning of iron and magnesium between basaltic liquids and pyroxenes is another potentially useful test of phenocryst–groundmass equilibrium. A partition coefficient $K_{dFe\text{-}Mg}^{Px\text{-}Liq}$ may be defined as $(X_{Cpx}^{FeO}/X_{Cpx}^{MgO} \cdot X_{Liq}^{MgO}/X_{Liq}^{FeO})$, analogous to that previously defined for partitioning of Fe^{2+} and Mg between olivine and melt. The calculation of $K_{dFe\text{-}Mg}^{Px\text{-}Liq}$ is complicated by the possible presence of ferric iron, not only in the melt phase but also in the Cpx. Grove & Bryan (1983), found that glass–phenocryst pairs from natural mid-ocean ridge basalts (MORBs) and experiments performed at 1 atm both suggest $K_{dFe\text{-}Mg}^{Px\text{-}Liq}$ that is ~0·23. No compositional dependence of $K_{dFe\text{-}Mg}^{Px\text{-}Liq}$ was inferred from their data but the lowest *mg*-number(melt) studied was 46, and thus the effect of low *mg*-number on partitioning was not constrained. Experiments by Hoover & Irvine (1977) in part of the system Mg_2SiO_4–Fe_2SiO_4–$CaMgSi_2O_6$–$CaFeSi_2O_6$–$KAlSi_3O_8$–SiO_2 covered a much larger range of *mg*-number(melt) and reported $K_{dFe\text{-}Mg}^{Px\text{-}Liq}$ values of 0·19–0·26, with a general decrease with falling *mg*-number(melt).

The calculated values of $K_{dFe\text{-}Mg}^{Px\text{-}Liq}$ from this study are shown in Fig. 17 as a function of the *mg*-number(melt); no consistent dependence of K_d on f_{O_2} is apparent. $K_{dFe\text{-}Mg}^{Px\text{-}Liq}$ varies between 0·18 and 0·26, with lower values at lower melt *mg*-number. These results agree with those of Hoover & Irvine (1977), and imply that the value of 0·23 suggested by Grove & Bryan (1983) is appropriate for partitioning of iron and magnesium between liquids and pyroxenes in basaltic systems. The relatively small effect of melt

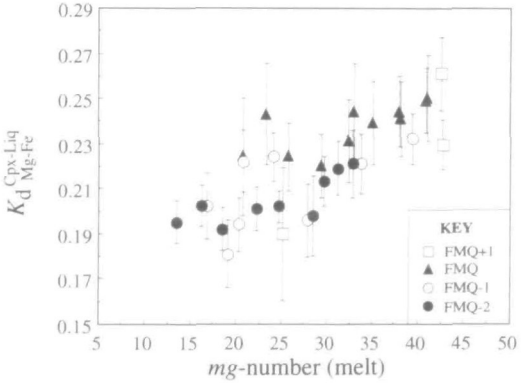

Fig. 17. The variation of $K_{dFe\text{-}Mg}^{Px\text{-}Liq}$ as a function of the *mg*-number of the melt. Both $K_{dFe\text{-}Mg}^{Px\text{-}Liq}$ and *mg*-number(melt) have been calculated taking into account the ferric iron content of the liquid, as estimated using Kilinc *et al.* (1983). The ferric iron content of the Cpx has been estimated from the stoichiometry of pyroxenes as discussed in the text. The error bars are estimated from the standard deviation of melts and pyroxenes shown in Table 2, but may be larger, particularly at FMQ + 1 where the ferric iron content of the Cpx is poorly constrained.

mg-number on Fe–Mg partitioning between pyroxene and melt is unlike that observed for olivine (cf. Figs 15a and 17) and may be related to the mixing of these elements on the M1 site of Cpx, which is known to be nearly ideal (Davidson & Lindsley, 1985).

Ca and Fe partitioning between pyroxene and melt

Calcium is a major component of both clinopyroxene and basaltic liquid, but Ca partitioning between pyroxene and liquid is rarely considered. Following the appearance of liquidus Cpx in our experiments the CaO content of the pyroxene, expressed as the wollastonite (Wo) component, decreases with falling temperature, and reaches a minimum before increasing again. The position of the Wo minimum shifts to lower *mg*-number(Cpx) with decreasing f_{O_2}, as shown in Fig. 8. This complex behaviour occurs despite the continuous decrease in melt CaO content with decreasing temperature, and the lack of effect of f_{O_2} on melt CaO content (Fig. 2d). Consideration of the molar ratios of iron and calcium in both the pyroxene and coexisting liquid (Fig. 18a) reveals a roughly linear relationship between them, which is independent of f_{O_2}. To verify whether this relation is true for a wide range of melt compositions the experimental data for $X_{Liq}^{CaO}/X_{Liq}^{FeO}$ and $X_{Cpx}^{CaO}/X_{Cpx}^{FeO}$ and from the work of Shi & Libourel (1991) and Shi (1992), for melts multiply saturated in Ol + Plag + Cpx in the system CaO–MgO–Al_2O_3–SiO_2–FeO, are shown in Fig. 18b. The experiments of Shi & Libourel (1991) and Shi (1992) cover a temperature range of 1220–1060°C, and both melt and pyroxene compositions range widely, from silica undersaturated to silica oversaturated. The large compositional range of these data supports the general applicability of our results for the covariation of $X_{Liq}^{CaO}/X_{Liq}^{FeO}$ and $X_{Cpx}^{CaO}/X_{Cpx}^{FeO}$ and and the observed correlation can be approximated by a first-order polynomial as shown in Fig. 18.

The observed relationship between Ca/Fe in clinopyroxene and Ca/Fe in the coexisting melt has several useful applications. A minimum in Wo content of Cpx is a common feature of natural tholeiitic rock series, including the Skaergaard intrusion (Wager & Brown, 1967). As noted above, the CaO content of the melt phase in systems cosaturated in Ol + Plag + Cpx generally decreases linearly with falling temperature (Helz, 1987; Shi & Libourel, 1991; this study). Thus, using the Fe–Ca relations shown in Fig. 18a, the observed variations in the CaO content of pyroxenes from natural systems may be explained in terms of the variation of FeO* content of the coexisting melts. The minimum in

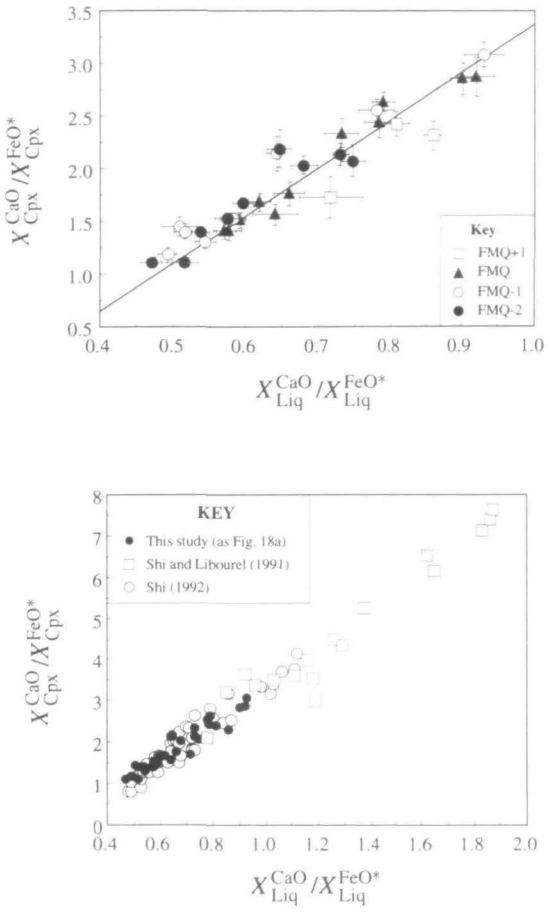

Fig. 18. (a) The covariation of the ratio of the mole fraction of CaO and FeO* in the experimental melts and high-calcium clinopyroxenes. The error bars have been calculated from the standard deviation of CaO and FeO* shown in Table 2. Neither of the ratios has been corrected for ferric iron. The ratio of calcium to iron in the pyroxene and liquid may be adequately described by a line ($y = 4{\cdot}54x - 1{\cdot}17$) as shown in the figure. (b) A comparison of the covariation of the ratio of the mole fraction of CaO and FeO* in the experimental melts and high-calcium clinopyroxenes from this study, with those obtained in the system CaO–MgO–Al_2O_3–SiO_2–FeO at 1 atm. Eighteen points come from the study of Shi & Libourel (1991), and 32 from the study of Shi (1992).

CaO(Cpx) is related to a maximum in FeO*(melt), and the position of the Wo minimum as a function of *mg*-number(Cpx) is related to the *mg*-number(melt) at the peak iron content. The presence of a Wo minimum in cumulate Cpx of the Skaergaard intrusion occurs following the saturation of the magma in magnetite, and may thus imply that a peak in iron enrichment did indeed occur at this time, as proposed by Hunter & Sparks (1987). Campbell & Nolan (1974) described tholeiitic rock series from the Sudbury, Jimberlana, Skaergaard, Bushveld and Bjerkrem–Sokndal layered intrusions. Each series shows a Wo minimum, but the positions of this minimum occur at different *mg*-number, covering the range from 75 to 20. If the different locations of the minima in Wo content of Cpx may be related to the appearance of magnetite on the liquidus, this provides a qualitative indication of the relative oxidation state of the magmas (because magnetite crystallizes at higher *mg*-number under more oxidizing conditions).

Na and Ca partitioning between plagioclase and melt

Plagioclase is one of the most common igneous minerals, and the partitioning of sodium and calcium between plagioclase and coexisting melt has been extensively used for geo-thermometry (e.g. Marsh *et al.*, 1990). However, common compositional zoning, and the potentially large influence of water activity on plagioclase–melt equilibria limit the use of plagioclase compositions as a test for phenocryst–groundmass equilibrium. Values of $K^{Plag\text{-}Liq}_{dCa\text{-}Na}$ [defined as $(X^{CaO}_{Plag}/X^{Na_2O}_{Plag} \cdot X^{Na_2O}_{Liq}/X^{CaO}_{Liq})$] from other studies of anhydrous sub-alkaline basalts typically range from 0·75 to 1·4 (Grove & Baker, 1984). Values of $K^{Plag\text{-}Liq}_{dCa\text{-}Na}$ from this study, shown in Fig. 19 as a function of melt *mg*-number, vary between 0·8 and 1·6 and show no systematic variation with melt *mg*-number. Consideration of potential errors owing to Na volatility during experiments and to slight zoning in plagioclase composition suggests that within error a single value of $1{\cdot}1 \pm 0{\cdot}2$ is consistent with the available data.

Cotectic proportions of crystalline phases

Over a given temperature interval the compositional evolution of the melt phase is controlled by the relative proportions and the compositions of the solid phases which have crystallized during that temperature interval, and estimation of cotectic proportions is thus essential for the modelling of ferro-basaltic

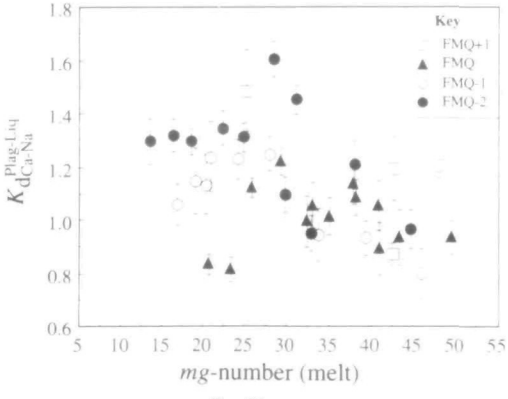

Fig. 19. The variation of $K^{Plag\text{-}Liq}_{dCa\text{-}Na}$ as a function of the *mg*-number of the melt. The error bars have been calculated from the standard deviation of CaO and Na_2O shown in Table 2.

differentiation trends (e.g. Toplis, 1994). During equilibrium crystallization the relative modal abundances of solid phases at a given temperature do not in general represent cotectic proportions, owing to the proportion of new phases on the liquidus being 'diluted' by existing crystals. The cotectic proportions of minerals produced by equilibrium crystallization may be estimated from variations in the abundances of the individual mineral phases with falling temperature (i.e. the relative gradients in Δ% mineral/ΔT from Figs 11–14). Figure 20 shows the studied T–f_{O_2} space divided into regions in which the stable crystallizing assemblage is fixed, using the inferred phase boundaries from Fig. 2, as well as the onset of the inferred olivine resorption reaction (Table 3, Fig. 12). Figures 11–14 show that within error, the calculated modal abundances of individual minerals increase linearly as temperature decreases for T–f_{O_2} paths parallel to the FMQ buffer at all f_{O_2} and temperature within each region defined in Fig. 20, with the notable exception of magnetite and olivine. Table 4 shows the calculated variations of mineral abundance as a function of temperature, and estimates of the 1σ error based on regression of data shown in Figs 11–14. These values have been used to calculate the relative crystallizing proportions of the stable minerals in each region for crystallization parallel to the FMQ buffer, and are also shown in Table 4. Because the high-temperature boundaries of clinopyroxene, magnetite and ilmenite are oblique to the f_{O_2} axis (Fig. 20) this implies that

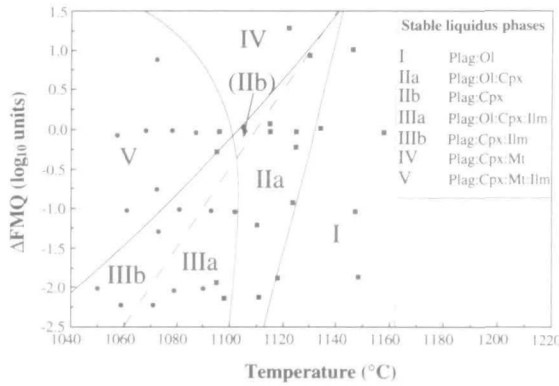

Fig. 20. A summary of the phase relations of the studied composition as a function of temperature and f_{O_2}. Each small symbol represents an experiment using either SC1 (squares) or SC4 (circles). The inferred phase boundaries are marked as continuous lines, and the dashed line marks the approximate onset of olivine resorption inferred from the variation of the absolute modal abundance of olivine as shown in Fig. 12. Regions II and III have therefore been divided into portions where olivine is a primary crystallizing phase (a), and a portion where olivine will not crystallize if the system crystallizes under conditions of fractional crystallization, or where olivine will resorb if the system crystallizes under conditions of equilibrium crystallization (b).

their modal abundances will depend not only on the temperature interval considered, but also on the change in ΔFMQ over that temperature interval. Quantification of these effects is beyond the scope of this paper, but must be considered when modelling basalt crystallization paths under conditions open and closed to oxygen (e.g. Toplis, 1994; Toplis & Carroll, unpublished).

Cotectic proportions of minerals forming in basaltic magmas have been obtained from (a) observation of natural cumulates, (b) measurements from experimental studies, and (c) modelling of major element variation in rocks from volcanic suites. Olivine + plagioclase is a common cumulus assemblage found in the lower parts of many basic intrusions (e.g. Rhum intrusion, Brown, 1956; Kiglapait intrusion, Morse, 1979), and the typical relative abundances of Ol_3:$Plag_7$ are excellent agreement with the results of this study (Table 4), and the experimental results of Grove & Baker (1984), for a basalt from the Galapagos spreading centre. The assemblage Ol–Plag–Cpx is also common in natural basalts, with typical (average) cotectic proportions of Ol_{15}:$Plag_{55}$:Cpx_{30} (Biggar, 1983). Results for basalts from the Oceanographer Fracture Zone (Shibata *et al.*, 1979), based on mass balance calculations, suggest crystallizing proportions of Ol_{12}:$Plag_{54}$:Cpx_{33}, and basalts from the Deccan Traps (Cox & Mitchell, 1988) suggest similar proportions in the range Ol_{10-15}:$Plag_{50-60}$:Cpx_{30-40}; these are in broad agreement with the experimental data from this study (Ol_{18}:$Plag_{50}$:Cpx_{32}), and from the experiments on a Galapagos basalt (Ol_{17}:$Plag_{58}$:Cpx_{25}; Grove & Baker,1984). Studies of simple basalt analogue systems CaO–MgO–Al_2O_3–SiO_2–FeO (Shi & Libourel, 1991; Shi, 1992) and CaO–MgO–Al_2O_3–SiO_2–Na_2O (Soulard, 1992) show that the crystallizing ratio of plagioclase to pyroxene in olivine-saturated melts is a sensitive function of the bulk composition, and this may in part explain the variability of the Plag:Cpx ratio in natural samples. Plagioclase is observed to be favoured over pyroxene for more silica-rich compositions, which may be explained by the increase in normative plagioclase at higher silica contents. The lower silica content of the composition SC1 used in this study (~48·5 wt % SiO_2) compared with that of the composition used by Grove & Baker (1984) (~51 wt % SiO_2), is consistent with the differences in inferred cotectic phase proportions.

Factors affecting Fe–Ti oxide crystallization

The crystallization of Fe–Ti oxides has a large influence on the compositional evolution of the coexisting

Table 4: Cotectic proportions

Region[a]	Ol	Pl	Cpx	Ilm	Mt
(a) Variation of mineral abundance as function of temperature (wt %/100°C)					
I	21(1)[b]	47(3)			
II	20(2)	53(3)	35(3)		
IIIa	18(2)	48(5)	48(3)	11(1)	
IIIb	res[c]	48(5)	48(3)	4(1)	
$IV_{d,e}$		48(5)	49(6)		18(4)
V_d		43(9)	49(6)		25(8)
(b) Crystallizing proportions (wt %)					
I	31(2)	69(5)	—	—	—
II	18(2)	50(4)	32(3)	—	—
IIIa	14(2)	38(4)	38(3)	9(1)	—
IIIb	res[c]	48(6)	48(4)	4(1)	
$IV^{d,e}$	—	42(5)	43(6)	—	15(4)
V^d	—	37(9)	42(7)	—	22(7)

[a] Refers to regions defined in Fig. 20. (For abbreviations of mineral names, see Table 3.)
[b] Numbers in parentheses represent 1σ errors.
[c] Olivine is not a stable phase and will resorb under conditions of equilibrium crystallization. The quoted value is taken from experiments at FMQ − 1, but is poorly constrained.
[d] The abundance of magnetite has been assumed to increase linearly with temperature, although the experimental data are not accurate enough to confirm this.
[e] Insufficient data are available to quantify the variation of mineral abundance with falling temperature. Extrapolations from adjoining regions have been made.

liquid, particularly the silica and iron contents (Fig. 4). Figure 2 shows that below ~1100°C Fe–Ti oxides are stable over the entire range of f_{O_2} investigated, but the identity of the stable Fe–Ti oxide is a sensitive function of f_{O_2}, with magnetite–ulvöspinel solid solution being stable at higher f_{O_2}, and ilmenite–haematite solid solution at lower f_{O_2}. The large positive $\Delta T/\Delta f_{O_2}$ slope of the magnetite liquidus reflects the dependence of Mt stability on oxidation state (and thus the ferric iron content of the liquid). Figure 21a shows that the ferric iron content of Mt-saturated melts [estimated using Kilinc *et al.* (1983)] is approximately a linear function of inverse temperature, independent of f_{O_2}. Although Toplis *et al.* (1994) have shown that in phosphorus-bearing melts, the calculated ferric iron contents of magnetite-saturated melts [using Kilinc *et al.* (1983)] increase with P_2O_5 content, even at fixed temperature (their fig. 11), comparison of the data from this study with those from magnetite-saturated melts reported by Juster *et al.* (1989), Snyder *et al.* (1993) and Thy & Lofgren (1994) (Fig. 21b) shows that within the uncertainties associated with the calculation scheme of Kilinc *et al.* (1983), the proposed relationship is broadly true. In detail, the gradient of the ferric-iron contents of magnetite-saturated melts as a function of inverse temperature is very similar for the melts produced in this study and by Juster *et al.* (1989), but is distinctly greater than that inferred for the melts produced in the experiments of Snyder *et al.* (1993) and Thy & Lofgren (1994). This may be qualitatively explained by the presence of phosphorus in the last two studies, and the lack of it in the former two. However, the data suggest that a simple relationship between temperature and the ferric iron content of magnetite-saturated melts exists, which is potentially useful for predicting the onset of magnetite crystallization.

The data from this study suggest that the crystallization of ilmenite as the first oxide phase is independent of oxidation state (Fig. 2), and is probably controlled by the melt TiO_2 content (Fig. 4a).

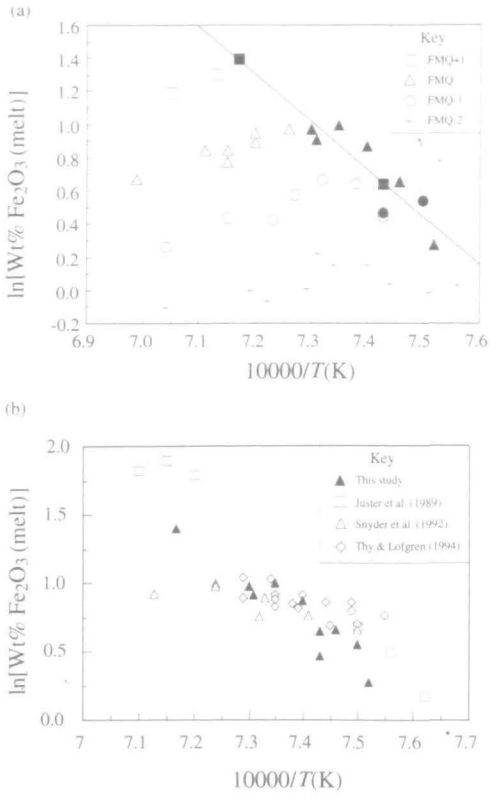

Fig. 21. (a) The variation of ln(wt % Fe_2O_3) of the melt as a function of inverse temperature. Experiments saturated in magnetite are signified by filled symbols. The data for magnetite-saturated melts may be described by the equation $y = -3{\cdot}19x + 24{\cdot}22$, which is independent of the f_{O_2} or proportion of magnetite, as shown in the figure. (b) A comparison of this study with data from the literature.

Ilmenite saturation at ~5·0 wt % TiO_2 and ~1100°C is consistent with data from a number of terrestrial systems which are inferred to crystallize ilmenite at very similar temperatures and TiO_2 contents (4·5–5·5 wt % TiO_2 at ~1100°C, e.g. Delong & Chatelain, 1990; Helz, 1987). At lower temperature the TiO_2 contents of melts from this study containing only ilmenite as an Fe–Ti oxide phase may be described as a linear function of temperature, which is supported by the data of Juster *et al.* (1989) and Thy & Lofgren (1994), as shown in Fig. 22.

Olivine stability and silica activity

Olivine resorption is a common feature of many silicate systems, and may significantly influence the evolution of melt composition during the differentiation of basaltic magmas (Helz, 1987; Juster *et al.*, 1989). Olivine resorption is generally considered to proceed by reactions involving the formation of either magnetite or the Mg–Fe component of pigeonite:

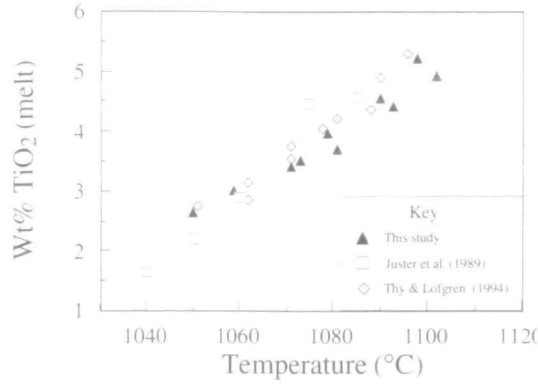

Fig. 22. The variation of wt % TiO_2 of ilmenite-saturated melts from this study, and data from the literature.

$$3Fe_2SiO_4^{Ol} + O_2 \leftrightarrow 2Fe_3O_4^{Mt} + 3SiO_2^{Liq} \quad (2)$$

$$Fe_2SiO_4^{Ol} + SiO_2^{Liq} \leftrightarrow 2FeSiO_3^{Pig}. \quad (3)$$

Although reaction (2) will be sensitive to the f_{O_2}, the activity of silica (a_{SiO_2}) will also influence the stability of olivine relative to magnetite and/or pigeonite. Qualitatively, in reducing conditions reaction (2) may not be able to pass to the right, but if the a_{SiO_2} is sufficiently high, destabilization of olivine may form pigeonite [reaction (3)]. Oxidation leads to the formation of magnetite, but also drives silication [reaction (2)] therefore promoting pigeonite stability [reaction (3)]. Both magnetite and pigeonite may be present, but at low a_{SiO_2} magnetite will be favoured [reaction (2)], whereas increasing the a_{SiO_2} will favour the formation of pigeonite [reaction (3)].

The resorption of olivine inferred from the results shown in Fig. 12 is not associated with the immediate precipitation of another crystalline phase, thus suggesting that neither of the above reactions is occurring and that olivine is in continuous reaction with the liquid. The onset of resorption, however, roughly parallels the magnetite liquidus, suggesting that a reaction of type (2) may be applicable. This implies that olivine is reacting to form a magnetite component in the liquid, rather than a magnetite component in the solid phase. A similar reaction of olivine with the liquid has been described by Shi & Libourel (1991) for reaction (3) in the vicinity of the pigeonite cotectic in the system CMAS + FeO. The lack of pigeonite in our experiments implies that reaction (2) dominates, and that the a_{SiO_2} is therefore relatively low and constant. The observed dependence of olivine resorption on f_{O_2} (see Fig. 12) is also consistent with the dominance of reaction (2). At oxidizing conditions, the activity of Fe_3O_4 in magnetite–ulvöspinel solid solution is greater than at reducing conditions. If a similar proportion of

'Fe_3O_4–Fe_2TiO_4' is formed at all f_{O_2} this therefore requires a larger proportion of olivine to be resorbed at higher f_{O_2}, in agreement with the experimental observations.

The data available from experimental studies and natural systems suggest that reactions (2) and (3) may both occur to varying degrees in typical ferro-basaltic melts. Examples may be found of systems which contain cumulus magnetite and no pigeonite (e.g. Kiglapait; Morse, 1979; this study), cumulus magnetite and intercumulus pigeonite (e.g. Skaergaard; McBirney, 1989), both magnetite and pigeonite as cumulus phases (e.g. Galapagos FeTi basalts; Juster *et al.*, 1989), and only pigeonite as a cumulus phase (e.g. CMAS + FeO system; Shi & Libourel, 1991). Given that all of these sources are inferred to have crystallized from very similar ferro-basaltic liquids, this implies that the reaction relations of olivine depend strongly on the oxygen fugacity and silica activity of the system.

CONCLUSIONS

The results of this experimental study document the effects of variable f_{O_2} on the phase equilibria and mineral and melt compositions of a ferro-basaltic composition. The f_{O_2} is found to have a large influence on the stability of the Fe–Ti oxides. The appearance temperature of the magnetite–ulvöspinel solid solution series is ~1100°C along the FMQ buffer, increasing by ~30°C per log f_{O_2} unit increase. Above the FMQ buffer magnetite is the first Fe–Ti oxide to appear on the liquidus, but below FMQ a member of the ilmenite–haematite solid solution is the first Fe–Ti oxide. Its appearance temperature of ~1100°C remains approximately constant between FMQ and FMQ − 2. Mass balance calculations and textural evidence suggest that olivine resorption occurs at all f_{O_2}, and that the onset of resorption roughly parallels the appearance of magnetite, occurring ~10°C higher. Consideration of the factors controlling the saturation of the Fe–Ti oxides suggests that the ferric iron content of magnetite-saturated melts is a linear function of inverse temperature. Similarly, the appearance temperature of ilmenite may be related to the TiO_2 content of the coexisting melt. Magnetite saturation results in immediate enrichment of the melt phase in SiO_2, and depletion in FeO*. Ilmenite saturation results in a similar enrichment in SiO_2, but iron enrichment in ilmenite-saturated melts may continue for ~10°C below the ilmenite liquidus. Experimental liquids reached a maximum of ~18 wt% FeO*, at ~48 wt% SiO_2, for ilmenite-saturated melts at low f_{O_2}, but more differentiated melts became depleted in iron and enriched in silica.

The effect of f_{O_2} on silicate mineral compositions and element partitioning between coexisting mineral–melt pairs is relatively small. In contrast, the compositions of both magnetite and ilmenite are sensitive functions of f_{O_2}, but show little variation in composition with temperature. Simple thermodynamic considerations of the distribution coefficients for iron and magnesium between olivines, pyroxenes and their coexisting iron-rich melts suggest that observed variations may be explained by non-idealities of Fe–Mg mixing in the crystalline phases, rather than non-idealities in the coexisting iron-rich melts. The measured partitioning of iron and calcium between Ca-rich clinopyroxene (Cpx) and melt suggests that a peak in the iron content of the melt with falling temperature may result in a minimum in wollastonite content of the Cpx (a common feature of many tholeiitic intrusions). Cotectic proportions for the assemblages Ol + Plag and Ol + Plag + Cpx estimated from mass balance calculations are found to be independent of temperature and f_{O_2}, and are in good agreement with values reported in the literature. The results suggest that the cotectic proportion of magnetite and ilmenite may be more complicated functions of both temperature and f_{O_2}.

These results provide indications of the compositions of the crystalline and melt products of ferro-basaltic differentiation, but are limited in application to the case of equilibrium crystallization. To be more relevant to natural systems an attempt must be made to consider the effects of fractional crystallization, and systems evolving closed to oxygen. The mineral proportions, distribution coefficients and factors affecting Fe–Ti oxide stability provided by the experiments described here may be used to model processes such as fractional crystallization and crystallization under conditions closed to oxygen, which are not easily investigated experimentally (Toplis, 1994; Toplis & Carroll, unpublished).

ACKNOWLEDGEMENTS

Fred Wheeler and Mike Overs are thanked for assistance in setting up the 1-atm furnaces, and Steve Lane for help with the microprobe at the University of Bristol. This work has benefited from numerous discussions with Jon Blundy, Al Davies, Guy Libourel, Henri Soulard and Bernie Wood, as well as critical reviews by S. A. Morse and an anonymous reviewer. M.J.T. acknowledges receipt of an NERC studentship during completion of this work.

REFERENCES

Albarède, F. & Provost, A., 1977. Petrological and geochemical mass-balance equations: an algorithm for least-square fitting and general error analysis. *Computers and Geosciences* **3,** 309–326.

Biggar, G. M., 1983. Crystallization of plagioclase, augite, and olivine in synthetic systems and in tholeiites. *Mineralogical Magazine* **47,** 161–176.

Brooks, C. K., Larsen, L. M. & Nielsen, T. F. D., 1991. Importance of iron-rich tholeiitic magmas at divergent plate margins: a reappraisal. *Geology* **19,** 269–272.

Brooks, C. K. & Nielsen, T. F. D., 1978. Early stages in the differentiation of the Skaergaard magma as revealed by a closely related suite of dike rocks. *Lithos* **11,** 1–14.

Brooks, C. K. & Nielsen, T. F. D., 1990. The differentiation of the Skaergaard Intrusion. A discussion of Hunter and Sparks. *Contributions to Mineralogy and Petrology* **104,** 244–247.

Brown, G. M., 1956. The layered ultrabasic rocks of Rhum, Inner Hebrides. *Philosophical Transactions of the Royal Society of London* **B240,** 1–53.

Byerly, G., 1980. The nature of differentiation trends in some volcanic rocks from the Galapagos spreading centre. *Journal of Geophysical Research* **85,** 3797–3810.

Campbell, I. H. & Nolan, J., 1974. Factors affecting the stability field of Ca-poor pyroxene and the origin of the Ca-poor minimum in Ca-rich pyroxenes from tholeiitic intrusions. *Contributions to Mineralogy and Petrology* **48,** 205–218.

Carmichael, I. S. E., 1964. The petrology of Thingmuli, a Tertiary volcano in eastern Iceland. *Journal of Petrology* **5,** 435–460.

Carmichael, I. S. E., 1991. The redox states of basic and silicic magmas: a reflection of their source region? *Contributions to Mineralogy and Petrology* **106,** 129–141.

Carmichael, I S. E. & Ghiorso, M. S., 1986. Oxidation–reduction relations in basic magma: a case for homogeneous equilibria. *Earth and Planetary Science Letters* **78,** 200–210.

Cox, K. G. & Mitchell, C., 1988. Importance of crystal settling in the differentiation of Deccan Trap basaltic magmas. *Nature* **333,** 447–449.

Davidson, P. M. & Lindsley, D. H., 1985. Thermodynamic analysis of quadrilateral pyroxenes. Part II: Model calibration from experiments and applications to geothermometry. *Contributions to Mineralogy and Petrology* **91,** 390–404.

Deines, P., Hafzinger, R. H., Ulmer, G. C. & Woermann, E., 1974. Temperature–oxygen fugacity tables for selected gas mixtures in the system C–H–O at one atmosphere total pressure. *Bulletin of the Earth and Mineral Sciences Experiment Station, Pennsylvania State University* **88,** 128.

Delong, S. E. & Chatelain, C., 1990. Trace-element constraints on accessory-phase saturation in evolved MORB magma. *Earth and Planetary Science Letters* **101,** 206–215.

Fornari, D. J., Perfit, M. R., Malahoff, A. & Embley, R., 1983. Geochemical studies of abyssal lavas recovered by DSRV Alvin from Eastern Galapagos Rift, Inca Transform, and Ecuador Rift. 1. Major element variations in natural glasses and spatial distribution of lavas. *Journal of Geophysical Research* **88,** 10519–10529.

Frost, B. R., Lindsley, D. H. & Anderson, D. J., 1988. Fe–Ti oxide–silicate equilibria: assemblages with fayalitic olivine. *American Mineralogist* **73,** 727–740.

Fudali, R. F., 1965. Oxygen fugacities of basaltic and andesitic magmas. *Geochimica et Cosmochimica Acta* **29,** 1063–1075.

Gee, L. & Sack, R. O., 1988. Experimental petrology of melilite nephelinites. *Journal of Petrology* **29,** 1233–1255.

Ghiorso, M. S. & Carmichael, I. S. E., 1985. Chemical mass transfer in magmatic processes. II. Applications in equilibrium crystallization, fractionation and assimilation. *Contributions to Mineralogy and Petrology* **90,** 121–141.

Grove, T. L., 1981. Use of FePt alloys to eliminate the iron loss problem in 1 atmosphere gas mixing experiments: theoretical and practical considerations. *Contributions to Mineralogy and Petrology* **78,** 298–304.

Grove, T. L. & Baker, M. B., 1984. Phase equilibrium controls on the tholeiitic versus calc-alkaline differentiation trends. *Journal of Geophysical Research* **89,** 3253–3274.

Grove, T. L. & Bryan, W. B., 1983. Fractionation of pyroxene-phyric MORB at low pressure: an experimental study. *Contributions to Mineralogy and Petrology* **84,** 293–309.

Helz, R. T., 1987. Differentiation behavior of Kilauea Iki lava lake, Kilauea Volcano, Hawaii: an overview of past and current work. In: Mysen, B. O. (ed.) *Magmatic Processes: Physiochemical Principles. Geochemical Society Special Publication* **1,** 241–258.

Hill, R. & Roeder, P., 1974. The crystallization of spinel from basaltic liquid as a function of oxygen fugacity. *Journal of Geology* **82,** 709–729.

Hoover, J. D. & Irvine, T. N., 1977. Liquidus relations and Mg–Fe partitioning on part of the system Mg_2SiO_4–Fe_2SiO_4–$CaMgSi_2O_6$–$CaFeSi_2O_6$–$KAlSi_3O_8$–SiO_2. *Carnegie Institute of Washington Yearbook* **77,** 774–784.

Huebner, J. S. & Sato, M., 1970. The oxygen fugacity–temperature relationships of manganese and nickel oxides buffers. *American Mineralogist* **55,** 934–952.

Hunter, R. H. & Sparks, R. S. J., 1987. The differentiation of the Skaergaard Intrusion. *Contributions to Mineralogy and Petrology* **95,** 451–461.

Hunter, R. H. & Sparks, R. S. J., 1990. The differentiation of the Skaergaard Intrusion. Reply to McBirney and Naslund. *Contributions to Mineralogy and Petrology* **106,** 248–254.

Jurewicz, A. J. G. & Watson, E. B., 1988. Cations in olivine, Part 1: Calcium partitioning and calcium–magnesium distribution between olivines and coexisting melts, with petrologic applications. *Contributions to Mineralogy and Petrology* **99,** 176–185.

Juster, T. C., Grove, T. L. & Perfit, M. R., 1989. Experimental constraints on the generation of Fe–Ti basalts, andesites, and rhyodacites at the Galapagos spreading centre, 85°W and 95°W. *Journal of Geophysical Research* **94,** 9251–9274.

Kennedy, G. C., 1948. Equilibrium between volatiles and iron oxides in igneous rocks. *American Journal of Science* **246,** 529–549.

Kilinc, A., Carmichael, I. S. E., Rivers, M. L. & Sack, R. O., 1983. The ferric–ferrous ratio of natural silicate liquids equilibrated in air. *Contributions to Mineralogy and Petrology* **83,** 136–140.

Leeman, W. P. & Scheidegger, K. F., 1977. Olivine/liquid distribution coefficients and a test for crystal–liquid equilibrium. *Earth and Planetary Science Letters* **35,** 247–257.

Le Roex, A. P., Dick, H. J. B., Reid, A. M. & Erlank, A. J., 1982. Ferrobasalts from the Spiess Ridge segment of the Southwest Indian Ridge. *Earth and Planetary Science Letters* **60,** 437–451.

Longhi, J. & Pan, V., 1988. A reconnaisance study of phase boundaries in low-alkali basaltic liquids. *Journal of Petrology* **29,** 115–147.

Marsh, B. D., Fournelle, J., Myers, J. D. & Chou, I-M., 1990. On plagioclase thermometry in island arc rocks: experiments and theory. In: Spencer, R. J. & Chou, I-M. (eds) *Fluid–Mineral Interactions: A Tribute to H. P. Eugster. Geochemical Society Special Publication* **1,** 65–83.

McBirney, A. R., 1989. The Skaergaard layered series: I. Structure and average compositions. *Journal of Petrology* **30,** 363–397.

McBirney, A. R. & Naslund, H. R., 1990. The differentiation of the Skaergaard Intrusion. A discussion of Hunter and Sparks. *Contributions to Mineralogy and Petrology* **104,** 235–240.

Morse, S. A., 1979. Kiglapait geochemistry: II. Petrography. *Journal of Petrology* **20,** 591–624.

Morse, S. A., 1981. Kiglapait geochemistry IV: the major elements. *Geochimica et Cosmochimica Acta* **45,** 461–479.

Morse, S. A., 1990. The differentiation of the Skaergaard Intrusion. A discussion of Hunter and Sparks. *Contributions to Mineralogy and Petrology* **104,** 240–244.

Muan, A. & Osborn, E. F., 1956. Phase equilibria at liquidus temperatures in the system MgO–FeO–Fe_2O_3–SiO_2. *Journal of the American Ceramic Society* **39,** 121–140.

O'Neill, H. StC., 1987. Quartz–fayalite–iron and quartz–fayalite–magnetite equilibrium and the free energy of formation of fayalite (Fe_2SiO_4) and magnetite (Fe_3O_4). *American Mineralogist* **72,** 67–75.

Osborn, E. F., 1959. Role of oxygen pressure in the crystallization and differentiation of basaltic magma. *American Journal of Science* **257,** 609–647.

Presnall, D. C., 1966. The join Forsterite–Diopside–Iron oxide and its bearing on the crystallization of basaltic and ultramafic magmas. *American Journal of Science* **264,** 753–809.

Roeder, P. L. & Emslie, R. F., 1970. Olivine–liquid equilibria. *Contributions to Mineralogy and Petrology* **29,** 275–289.

Roeder, P. L. & Osborn, E. F., 1966. Experimental data for the system MgO–FeO–Fe_2O_3–$CaAl_2Si_2O_8$–SiO_2 and their petrological implications. *American Journal of Science* **264,** 428–480.

Sack, R. O., Carmichael, I. S. E., Rivers, M & Ghiorso, M. S., 1980. Ferric–ferrous equilibria in natural silicate liquids at 1 bar. *Contributions to Mineralogy and Petrology* **75,** 369–376.

Sato, M., 1978. Oxygen fugacity of basaltic magmas and the role of gas-forming elements. *Geophysical Research Letters* **5,** 447–449.

Shi, P., 1992. Basalt evolution at low pressure: implications from an experimental study in the system CaO–FeO–MgO–Al_2O_3–SiO_2. *Contributions to Mineralogy and Petrology* **110,** 139–153.

Shi, P., 1993. Low-pressure phase relationships in the system Na_2O–CaO–FeO–MgO–Al_2O_3–SiO_2 at 1100°C with implications for the differentiation of basaltic magmas. *Journal of Petrology* **34,** 743–762.

Shi, P. & Libourel, G., 1991. The effects of FeO on the system CMAS at low pressure and implications for basalt crystallization processes. *Contributions to Mineralogy and Petrology* **108,** 129–145.

Shibata, T., Delong, S. E. & Walker, D., 1979. Abyssal tholeiites from the Oceanographer Fracture Zone. *Contributions to Mineralogy and Petrology* **70,** 89–102.

Snyder, D. & Carmichael, I. S. E., 1992. Olivine–liquid equilibria and the chemical activities of FeO, NiO, Fe_2O_3, and MgO in natural basic melts. *Geochimica et Cosmochimica Acta* **56,** 303–318.

Snyder, D., Carmichael, I. S. E. & Wiebe, R. A., 1993. Experimental study of liquid evolution in an Fe-rich, layered mafic intrusion: constraints of Fe–Ti oxide precipitation on the T–f_{O_2}, and T–ρ paths of tholeiitic magmas. *Contributions to Mineralogy and Petrology* **113,** 73–86.

Soulard, H., 1992. Evolution des laves basiques alcalines étude expérimentale à 1 atmosphere du système analogue synthetique CaO–MgO–Al_2O_3–SiO_2–Na_2O (CMASN). Ph.D. Thesis, Université Blaise Pascal, Clermont-Ferrand.

Sparks, R. S. J., Meyer, P. & Sigurdsson, H., 1980. Density variation amongst mid-ocean ridge basalts: implications for magma mixing and the scarcity of primitive lavas. *Earth and Planetary Science Letters* **46,** 419–430.

Stolper, E. & Walker, D., 1980. Melt density and the average composition of basalt. *Contributions to Mineralogy and Petrology* **74,** 7–12.

Stormer, J. C., Jr, 1983. The effects of recalculation on estimates of temperature and oxygen fugacity from analyses of multicomponent iron–titanium oxides. *American Mineralogist* **68,** 586–594.

Thy, P. & Lofgren, G. E., 1994. Experimental constraints on the low-pressure evolution of transitional and mildly alkalic basalts: the effect of Fe–Ti oxide minerals and the origin of basaltic andesites. *Contributions to Mineralogy and Petrology* **116,** 340–351.

Toplis, M. J., 1994. The origin of iron-rich igneous rocks: an experimental study. Ph.D. Thesis, University of Bristol.

Toplis, M. J., Libourel, G. & Carroll, M. R., 1994. The role of phosphorus in the crystallisation processes of basalt: an experimental study. *Geochimica et Cosmochimica Acta* **58,** 797–810.

Tormey, D. R., Grove, T. L. & Bryan, W. B., 1987. Experimental petrology of normal MORB near the Kane Fracture Zone: 22°–25°N, mid-Atlantic ridge. *Contributions to Mineralogy and Petrology* **96,** 121–139.

Wager, L. R., 1960. The major element variation of the layered series of the Skaergaard intrusion and a re-estimation of the average composition of the hidden layered series and of the successive residual magmas. *Journal of Petrology* **1,** 364–398.

Wager, L. R. & Brown, G. M., 1967. *Layered Igneous Rocks.* Edinburgh: Oliver and Boyd, 558 pp.

Wager, L. R. & Deer, W. A., 1939. Geological investigations in East Greenland. III. The petrology of the Skaergaard intrusion, Kangerdlugssuag, East Greenland. *Meddelelser om Grønland* **105,** 1–352.

Walker, D., Shibata, T. & DeLong, S. E., 1979. Abyssal tholeiites from the Oceanographer Fracture Zone II, phase equilibria and mixing. *Contributions to Mineralogy and Petrology* **70,** 111–115.

Williams, R. J., 1971. Reaction constants in the system FeO–MgO–SiO_2–O_2; intensive parameters in the Skaergaard intrusion, East Greenland. *American Journal of Science* **271,** 132–146.

Wiser, N. M. & Wood, B. J., 1991. Experimental determination of activities in Fe–Mg olivine at 1400 K. *Contributions to Mineralogy and Petrology* **108,** 146–153.

Wood, B. J. & Virgo, D., 1989. Upper mantle oxidation state: ferric iron contents of lherzolite spinels by ^{57}Fe Mössbauer spectroscopy and resultant oxygen fugacities. *Geochimica et Cosmochimica Acta* **53,** 1271–1291.

RECEIVED NOVEMBER 28, 1994
REVISED TYPESCRIPT ACCEPTED FEBRUARY 8, 1995